Science of Remote Sensing 14 (2026) 100482

Contents lists available at ScienceDirect

Science of Remote Sensing

journal homepage: www.sciencedirect.com/journal/science-of-remote-sensing

Monitoring post-fire ecohydrological recovery through integrated remote sensing and ecological modeling

Yulong Zhang [a,*], Wenhong Li [a], Peter V. Caldwell [b], Steven P. Norman [c], Conghe Song [d], Ge Sun [e,**]

[a] Division of Earth and Climate Sciences, Nicholas School of the Environment, Duke University, Durham, NC, USA
[b] Center for Integrated Forest Science, Southern Research Station, USDA Forest Service, Otto, NC, 28763, USA
[c] Eastern Forest Environmental Threat Assessment Center (EFETAC), Southern Research Station, USDA Forest Service, Asheville, NC, USA
[d] Department of Geography and Environment, University of North Carolina at Chapel Hill, Chapel Hill, NC, USA
[e] Eastern Forest Environmental Threat Assessment Center (EFETAC), Southern Research Station, USDA Forest Service, Raleigh, NC, USA

ARTICLE INFO

Keywords:
Post-fire recovery
Harmonized Landsat Sentinel-2
Coupled Carbon–Water model
Burn severity
Ecohydrological modeling
Carbon-water-erosion

ABSTRACT

Wildfire simultaneously disrupts ecosystem carbon, water, and soil processes, yet these coupled effects and post-fire recovery trajectories cannot be reliably assessed from spectral vegetation indices alone. Here, we developed a fine-scale, multi-dimensional framework to quantify wildfire impacts and post-fire ecohydrological recovery, using the 2016 megafire in Great Smoky Mountains National Park in the eastern United States as a testbed. This framework integrated gap-filled 30 m NASA Harmonized Landsat and Sentinel-2 surface reflectance with an expanded diagnostic ecosystem model (Coupled Carbon and Water Model) to generate spatially consistent estimation of gross primary productivity (GPP), evapotranspiration (ET), water yield (WY), and soil erosion (SE) from 2014 to 2024 within Google Earth Engine. Fire effects were isolated from climate variability using pixel-level counterfactual simulations that produced no-fire baselines under identical meteorological forcing. We found that GPP declined by 20.7%, ET by 20.0%, WY increased by 19.2%, and soil erosion increased 12.5 times in the first post-fire year. Recovery trajectories varied strongly with burn severity, with high-severity patches retaining persistent modeled functional deficits (−13% GPP, −9% ET, +9% WY, and 5× SE) after eight years despite full spectral recovery (NDVI +2%). Our findings reveal a distinct decoupling between spectral recovery and the modeled carbon, water, and erosion responses, driven by incomplete ecological succession, where high-severity areas remain in herb- and shrub-dominated stages rather than recovering to forest. The severity-stratified diagnostic framework we provide offers a directly applicable tool for post-fire vegetation assessment, hydrological response monitoring, and long-term restoration planning in fire-affected ecosystems.

1. Introduction

Wildfire regimes are intensifying across the globe, with increasing fire frequency, extent, and severity driven by rising temperatures, prolonged drought, and accumulating fuel loads (Bowman et al., 2009, 2020; Abatzoglou and Williams, 2016). Beyond direct vegetation loss, fire simultaneously disrupts multiple ecosystem functions, such as suppressing carbon uptake, altering water partitioning, and destabilizing soils, making it a nexus disturbance with cascading consequences for ecosystem health, watershed hydrology, and downstream water quality (Seidl et al., 2017; McDowell et al., 2020). These impacts propagate through tightly coupled ecohydrological pathways, as canopy loss reduces photosynthesis, interception, and transpiration, increasing overland flow and exposing mineral soils to rainfall erosivity and accelerated erosion (Moody et al., 2013; Xu et al., 2024; Zhang et al., 2025a; Vieira et al., 2026). Yet most post-fire studies examine carbon, water, or soil processes in isolation for immediate mitigation, leaving the long-term coupled trajectories of ecosystem recovery poorly constrained (Bowman et al., 2020; Zacharakis and Tsihrintzis, 2026).

A key obstacle to understanding functional recovery is the widespread reliance on spectral vegetation indices (VIs) from optical remote sensing such as Normalized Difference Vegetation Index (NDVI) and

* Corresponding author.
** Corresponding author.
E-mail addresses: yulong.zhang@duke.edu (Y. Zhang), ge.sun@usda.gov (G. Sun).

https://doi.org/10.1016/j.srs.2026.100482
Received 31 March 2026; Received in revised form 16 July 2026; Accepted 3 August 2026
Available online 4 August 2026

Normalized Burn Ratio (NBR) as proxies for ecosystem state in both research and operational monitoring (Gitas et al., 2012; Pérez-Cabello et al., 2021). While these indices effectively capture canopy greenness and correlate with burn severity as measured in the field, a growing body of evidence highlights a persistent gap between optical signals and ecosystem function. Early successional vegetation can exhibit rapid green up that closely resembles pre-fire spectral conditions, even while carbon assimilation efficiency, transpiration capacity, and soil stability remain substantially impaired (Bright et al., 2019; Lv et al., 2025; Qiu et al., 2026). Long-term studies further show that recovery of forest structure and carbon stocks can lag for decades following stand-replacing fires, and that canopy greenness can conceal compositional shifts, such as shrub or early successional deciduous forest, that fundamentally alter ecosystem function even when spectral indices appear recovered (Kiel et al., 2025). These discrepancies extend beyond carbon dynamics. Post fire reductions in evapotranspiration lead to increased water yield through changes in the water balance (Smith et al., 2011; Wine et al., 2018; Hallema et al., 2018), while canopy loss and altered soil conditions can sustain elevated erosion risk long after optical indices suggest recovery (Moody et al., 2013; Jackson et al., 2018; Vieira et al., 2026). Together, these lines of evidence indicate that VI-based assessments may systematically underestimate the duration and magnitude of disruption in productivity, ET, water yield, and erosion, the key variables that govern ecosystem resilience and services.

Most evidence for spectral–functional decoupling post-fire has emerged from conifer ecosystems in the western U.S., where stand-replacing crown fires and regeneration limitations produce prolonged and visually conspicuous recovery trajectories (Stevens-Rumann and Morgan, 2019; Rodman et al., 2020; Nolan et al., 2021). Temperate forests of the eastern U.S., by contrast, remain comparatively underrepresented in integrated post-fire carbon–water–erosion research, despite their ecological importance, high biodiversity, and distinct disturbance–recovery dynamics (Allen et al., 2015; Seidl et al., 2017). The 2016 Chimney Tops 2 (CT2) wildfire in Great Smoky Mountains National Park (GSMNP) in the eastern U.S. offers a valuable testbed for examining how fire reshapes carbon, water, and erosion dynamics in a temperate mountain ecosystem. GSMNP's mixed resprouting and recruitment forest can green up rapidly enough to mask persistent functional deficits, with visible canopy recovery resuming within seasons even while carbon uptake and ET remain suppressed and structural and functional recovery proceed on different trajectories (S.C. Beals et al., 2022; Bouvier et al., 2025). High-severity fire here also carries outsized conservation consequences, since altered old-growth forests, disrupted understory communities, and reduced habitat connectivity can persist long after canopy closure, with lasting implications for biodiversity and adaptive management in one of North America's most species-rich protected areas (Noss et al., 2006). These ecological stakes are further compounded by the site's physical geography, where steep terrain and high rainfall erosivity intensify post-fire soil destabilization and elevate both sediment mobilization and water yield, making GSMNP a particularly informative setting for examining wildfire's multi-dimensional functional legacy.

Recent advances in satellite remote sensing and ecosystem modeling have created new opportunities to assess fire impacts on ecosystem functions. NASA's Harmonized Landsat–Sentinel-2 (HLS) dataset merges observations from two independent satellite constellations into a consistent 30-m surface reflectance time series at roughly 2-3 day revisit frequency, enabling gap-filled reconstruction of fine-scale vegetation dynamics across burn-severity mosaics (Claverie et al., 2018). Cross-calibrated radiometry and a common grid ensure that spectral indices from Landsat and Sentinel-2 are directly interchangeable, while the dense temporal sampling is essential for tracking the rapid and heterogeneous recovery signals that characterize post-fire vegetation in cloud-prone montane environments like GSMNP.

Translating these satellite observations into functional ecosystem estimates, however, requires a modeling framework that explicitly couples carbon and water fluxes. The Coupled Carbon–Water (CCW) model meets this requirement by linking gross primary production (GPP) and evapotranspiration (ET) through shared carbon–water constraints and has been evaluated from regional to global scales based on global eddy flux data and watershed streamflow data (Zhang et al., 2016, 2019, 2025b). Because CCW derives GPP and ET from land cover and biome-specific vegetation parameters rather than greenness alone, it is considerably more robust for post-fire recovery assessment than index-based approaches. An important methodological consideration is that fire-effect estimates are sensitive to how reference conditions are defined, given that recovery trajectories are strongly modulated by post-fire climate anomalies (Bright et al., 2019) and climatically unrepresentative baselines can substantially bias inferred fire effects (Meng et al., 2015). This sensitivity motivates explicit comparison among counterfactual, before-after, and spatial-reference approaches.

Here, we extended CCW to version 2.0 by incorporating the Revised Universal Soil Loss Equation (RUSLE), enabling simultaneous and spatially consistent estimation of GPP, ET, water yield (WY), and soil erosion (SE) at a 30-m resolution within the Google Earth Engine (GEE) platform. Rather than replacing spectral indices, this framework retains vegetation index as a core input and embeds it within physical carbon, water, and erosion constraints, so that greenness is interpreted through ecosystem function rather than equated with it. This study pursues four objectives: (1) develop and validate CCW 2.0 against independent NEON eddy-covariance and USGS streamflow observations; (2) quantify immediate and post-fire recovery trajectories (2017-2024) across burn-severity classes for GPP, ET, WY, and SE; (3) characterize the coupling and decoupling of greenness, carbon, water, and erosion responses as indicators of nexus recovery; and (4) compare counterfactual, before–-after, and spatial reference methods for attributing fire effects and evaluate their sensitivity to climate confounding. Findings from this work carry broad implications for post-fire ecosystem monitoring, restoration prioritization, watershed management, and the design of early-warning systems for downstream sediment and water-quality hazards in similar fire-affected landscapes. More broadly, the fire severity-stratified, multi-dimensional framework developed here offers a transferable approach for land managers and conservation agencies seeking to move beyond VI-based assessments toward functionally grounded, spatially explicit monitoring of disturbance recovery across protected and publicly managed forest landscapes.

2. Materials and methods

2.1. Study area

Great Smoky Mountains National Park (GSMNP) lies in the southern Appalachian Mountains along the Tennessee–North Carolina border in the eastern U.S. (Fig. 1a), with a total area of 2114 km^2 (National Park Service, 2025). Elevations span 267 m to 2025 m, creating strong topographic controls on temperature and moisture, with mean annual precipitation increasing from ~1400 mm yr^{-1} in lowlands to ~2160 mm yr^{-1} on high ridges (National Park Service, 2025). GSMNP is internationally recognized for exceptional temperate-zone biodiversity. As a United Nations Educational, Scientific and Cultural Organization (UNESCO) World Heritage Site, it is described as supporting >3500 plant species and ~130 native tree species, nearly as many as in all of Europe (UNESCO World Heritage Centre, 2012).

The 2016 Chimney Tops 2 fire (CT2), ignited on 23 November in the steep, rugged terrain near Chimney Tops and burned for approximately one month, provides a rare and valuable eastern U.S. test case for post-fire recovery in a mesic, high-biomass forest ecosystem (National Park Service, 2022). Under an acute late-fall drought and a rare mountain wave wind event (Williams et al., 2025), the fire exhibited extreme behavior and produced large high-severity patches, with severe impacts extending into the adjacent wildland–urban interface near Gatlinburg,

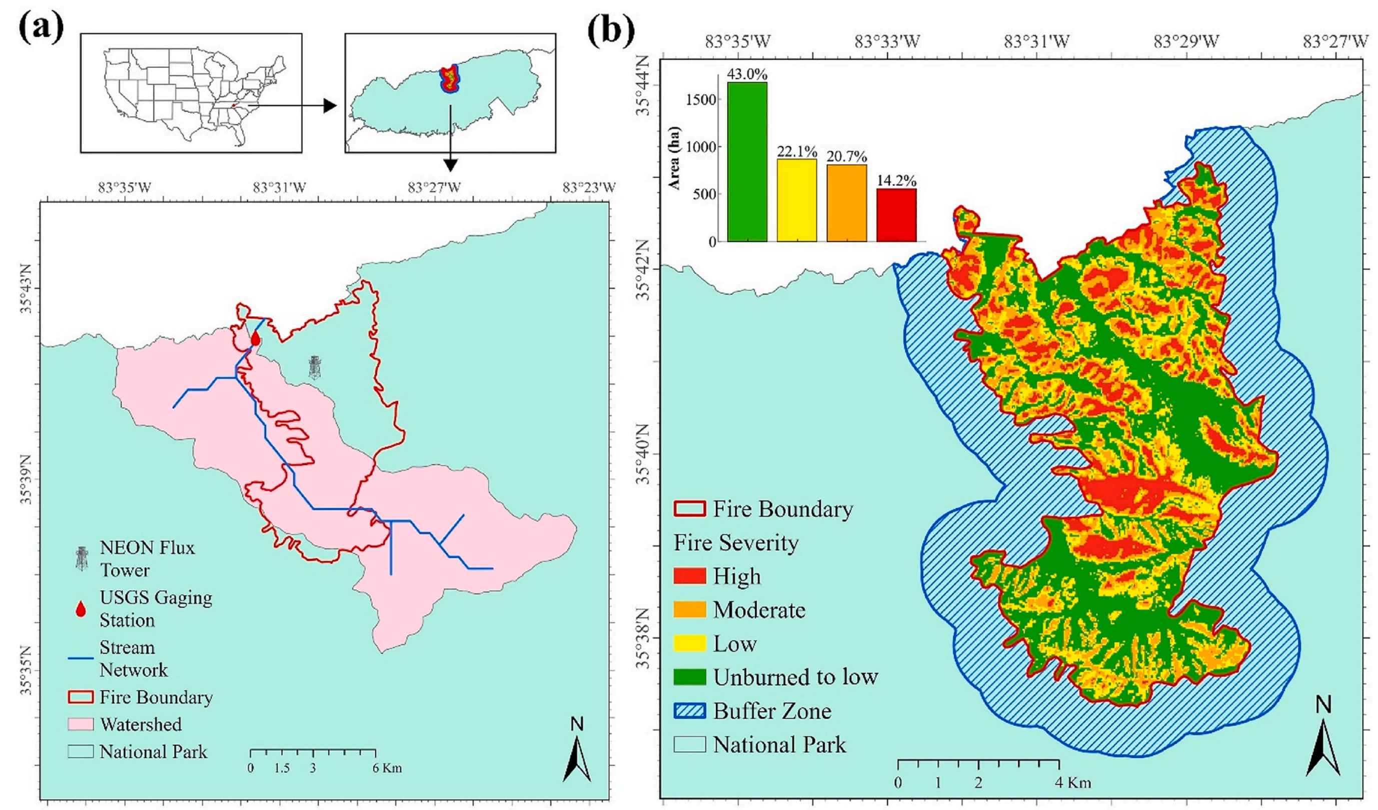

Fig. 1. Spatial distribution of fire severity, watershed characteristics, and locations of validation sites within and surrounding the 2016 Chimney Tops 2 fire in Great Smoky Mountains National Park. **(a)** Watershed delineation and ground-based measurement locations within the study domain. Pink shading indicates the watershed extent delineated by the USGS streamflow gaging station, the red outline marks the fire perimeter, and the light green area denotes the national park. Blue lines depict the stream network, with the locations of the NEON eddy covariance flux tower and USGS streamflow gaging station indicated by corresponding symbols. **(b)** Burn severity classification derived from remote sensing (see method section 2.2.2), with severity levels indicated as high (red), moderate (orange), low (yellow), and unburned-to-low (green). The red outline delineates the fire perimeter from MTBS, the blue hatched area marks the 1-km buffer zone surrounding the fire boundary, and the light green background represents the national park. The inset map shows the location of the study area within the southeastern United States. The bar plots show the area fraction of each severity class.

Tennessee (Reilly et al., 2022). We delineated the burned study domain within the park (Fig. 1b) using the Monitoring Trends in Burn Severity (MTBS) perimeter (Eidenshink et al., 2007), which captures approximately 4000 ha mixed severity burn mosaic for CT2 (Park and Sim, 2023).

2.2. Remote sensing data

2.2.1. Gap-filled NDVI from Harmonized Landsat Sentinel-2 (HLS) surface reflectance

We utilized HLS version 2.0 to derive continuous vegetation dynamics at 30-m resolution across the full study period (January 2014–December 2024). HLS harmonizes Landsat 8/9 OLI and Sentinel-2A/B MSI observations through a multi-step processing pipeline that includes atmospheric correction, cloud and shadow masking (Fmask), bidirectional reflection disturbance function (BRDF) normalization to a common sun-sensor geometry, spectral bandpass adjustment, and sub-pixel spatial co-registration (Claverie et al., 2018), yielding a sub-weekly revisit frequency at mid-latitudes. Data were accessed and processed through Google Earth Engine (Gorelick et al., 2017). NDVI was derived from HLS surface reflectance and used to calculate fraction of photosynthetically active radiation (FPAR) as the primary input to CCW 2.0 (Section 2.3); however, observations flagged by Fmask for cloud, cloud shadow, adjacent cloud, snow/ice, or aerosol contamination were excluded, introducing spatiotemporal gaps that required gap-filling prior to model application.

Temporally continuous monthly time series were generated through a three-stage gap-filling procedure designed to maximize spatial completeness while preserving phenological signal integrity. First, clear observations were composited into weekly maximum-value composites to regularize the irregular HLS acquisition schedule, then smoothed using a locally weighted moving-window filter (Chen et al., 2004, 2021). The filter computes the smoothed NDVI value at week i as a locally weighted average within a moving window (set W = 11 weeks here):

$$\widehat{x}_i = \frac{\Sigma_{k=a}^{b} w_k \cdot g(|k-i|) \cdot x_k}{\Sigma_{k=a}^{b} w_k \cdot g(|k-i|)} \tag{1}$$

where $a = \max(0, i - \lfloor W/2 \rfloor)$ and $b = \min(N-1, i + \lfloor W/2 \rfloor)$ define the window bounds, x_k is the weekly NDVI composite at week k, w_k is the observation-dependent quality weight, and $g(d)$ is a Gaussian distance kernel:

$$g(d) = exp\left(-\frac{d^2}{\lambda}\right) \tag{2}$$

with smoothing parameter $\lambda = 100$. The quality weights are assigned based on NDVI magnitude (x_k) to suppress residual cloud contamination while preserving phenological maxima ($w_k = 0.5$ for $x_k < 0.3$; $w_k = 1.0$ for $0.3 \le x_k < 0.6$; $w_k = 2.0$ for $x_k \ge 0.6$). Smoothed weekly values were then aggregated to monthly means.

Second, remaining monthly gaps of up to three consecutive months were filled using distance-weighted linear interpolation between the nearest preceding and following valid observations. For interior gaps, a gap at month j bounded by valid observations at months j_F (nearest preceding) and j_B (nearest following) is filled as:

$$\hat{x}_j = \frac{d_B}{d_F + d_B} \cdot x_{jF} + \frac{d_F}{d_F + d_B} \cdot x_{jB} \tag{3}$$

where $d_F = j - j_F$ and $d_B = j_B - j$ are the temporal distances to the forward and backward anchors, respectively. Interpolation is applied only when the total gap size $(d_F + d_B) \leq 3$ months. For edge gaps where only one anchor is available, the single valid neighbor is carried forward or backward provided the distance does not exceed 3 months.

Third, pixels still lacking valid values were filled using a climatological approach with explicit period-separation rules to prevent contamination across the fire boundary. For pre-fire years (2014–2016), fill values were drawn exclusively from other pre-fire years within a ±5-year window; for post-fire years (2018–2024), fill values were drawn exclusively from other post-fire years. For the fire year (2017), gaps were filled sequentially from 2018, then 2019, and finally from the post-fire period mean. This hierarchical fill strategy ensured that the immediate post-fire NDVI signal was preserved rather than diluted by pre-fire conditions. This period-separation rule prevented artificial smoothing of the fire-induced NDVI discontinuity that would otherwise occur if pre- and post-fire observations were pooled in the gap-filling climatology.

The resulting product is a spatially complete monthly NDVI dataset at 30-m resolution for 2014–2024, serving roles as the primary vegetation index for burn severity analysis, model running and spatial reference comparisons. As a test over a representative burned pixel (Fig. 2), quality-weighted smoothing reconstructed the seasonal trajectory from high-quality observations, preserved the post-fire vegetation decline, and corrected the low bias caused by residual cloud and haze when all observations were included. At the spatial scale, gap filling corrected the underestimation of annual NDVI derived from high-quality observations alone, which results from missing monthly data (Fig. S1). Data gaps, and therefore reliance on gap filling, were greatest at high elevations (Fig. S1a), where persistent orographic clouds and fog most strongly limit clear-sky observations. Although these areas coincide with upper-elevation high-severity burn patches, differences between gap-filled and clear-sky NDVI remained small and showed little systematic bias (Fig. S1e and f).

2.2.2. Burn severity mapping

Fire severity was mapped using the differenced Normalized Burn Ratio (dNBR) derived from Landsat 8 OLI surface reflectance, where NBR was computed as:

$$NBR = \frac{\rho_{NIR} - \rho_{SWIR2}}{\rho_{NIR} + \rho_{SWIR2}} \tag{4}$$

using bands B5 (NIR) and B7 (SWIR2). Pre- and post-fire median growing-season composites (April–October 2016 and April–October 2017) were generated from cloud- and shadow-masked imagery, and fire-induced change was quantified as:

$$dNBR = NBR_{pre\text{-}fire} - NBR_{post\text{-}fire} \tag{5}$$

dNBR was classified into four severity classes following established thresholds (Key and Benson, 2006): unburned-to-low (dNBR < 0.1), low severity (0.1 ≤ dNBR < 0.27), moderate severity (0.27 ≤ dNBR < 0.66),

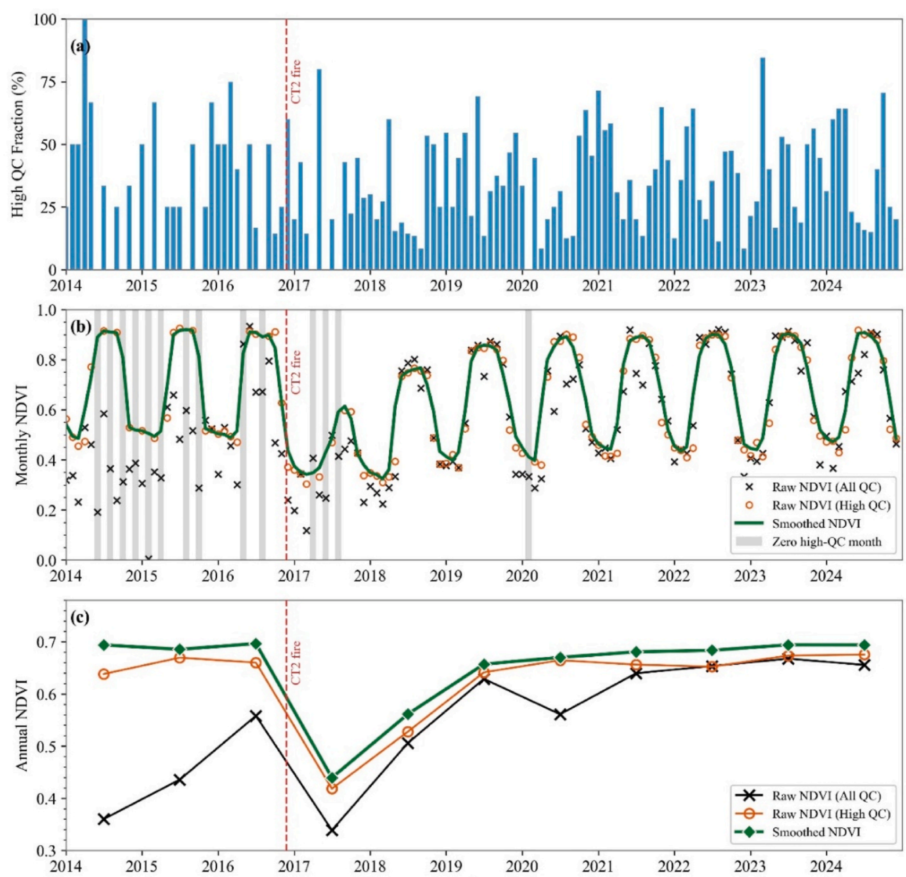

Fig. 2. Quality control and temporal smoothing of the HLS NDVI time series for a representative burned pixel (2014–2024). **(a)** Monthly fraction of high-quality (classified as clear by Fmask) NDVI observations relative to all available observations. **(b)** Monthly NDVI derived from all observations (black ×), high-quality observations only (orange circles), and the quality-weighted temporally smoothed series (green line). Grey shading indicates months with no high-quality observations that need to be gap-filled based on nearby data. **(c)** Annual mean NDVI calculated from all observations (black), high-quality observations only (orange), and the smoothed series (green). The vertical dashed line denotes the 2016 Chimney Tops 2 (CT2) wildfire. The location of the test pixel is shown in Fig. S1.

and high severity (dNBR $\geq$ 0.66). We used growing-season composites rather than differencing the near-date scenes used by MTBS fire severity product. Since the CT2 fire burned in the dormant season, near-date differencing contrasts two leaf-off canopies and captures little of the effect on active vegetation, whereas growing-season differencing better reflects the fire's ecological impact (Keeley, 2009; Cansler and McKenzie, 2012). We retained the MTBS fire perimeter and used a 1-km external buffer around it (Fig. 1b) as an unburned neighbor reference for the spatial-reference comparison (Section 2.5).

2.2.3. Land cover, meteorological and ancillary data

Land-cover classifications were derived from the Annual National Land Cover Database (NLCD) product at 30-m resolution from 2014 to 2024. To match the plant functional types for which the CCW model is parameterized (see Section 2.3.1), the NLCD classes were aggregated into five vegetation classes: evergreen forest, deciduous forest, mixed forest, shrub (shrub/scrub and woody wetlands), and grass/herbaceous (grassland/herbaceous, pasture/hay, and emergent herbaceous wetlands); non-vegetated classes (water, developed, barren, ice/snow, and cropland) were masked out. This annual series provides the biome-specific model parameters and underpins the post-fire land-cover-transition analysis (Fig. S2).

Daily meteorological forcing including minimum and maximum temperature, precipitation, vapor pressure deficit (VPD), and shortwave radiation were obtained from Daymet Version 4 at 1-km resolution (Thornton et al., 2022). Elevation and terrain derivatives were computed from the USGS 3DEP/National Elevation Dataset (1/3 arc-second). Soil inputs were derived from the POLARIS dataset (Probabilistic Remapping of SSURGO), which provides 30-m probabilistic soil property maps across CONUS (Chaney et al., 2019). From POLARIS, we used mean estimates of bulk density, texture fractions (sand, silt, clay), organic matter, and saturated hydraulic conductivity to parameterize soil and erosion-related properties (see Section 2.3.2).

2.3. Remote sensing-driven eco-hydrological modeling

2.3.1. Coupled Carbon–water model (CCW)

The Coupled Carbon–Water model (CCW) is a diagnostic, observation-driven framework that estimates GPP and ET from satellite-observed vegetation state and meteorological forcing (Zhang et al., 2016, 2019, 2025b). To clarify the multivariable framework, we distinguished the observed inputs, including HLS derived NDVI, Daymet meteorology, and static soil and terrain properties, from the diagnosed outputs, including GPP, ET, WY, and SE. These outputs are model estimates calculated from the inputs using the equations below rather than independent measurements. The model is intentionally parsimonious and diagnostic, using a small set of biome specific parameters listed in Table S1 instead of extensive free parameter calibration. This structure keeps the full carbon, water, and erosion pathway traceable to a common vegetation and climate basis.

In CCW, GPP is estimated as the product of absorbed photosynthetically active radiation (APAR) and realized light use efficiency (ε):

$$GPP = APAR \times \varepsilon = (PAR \times FPAR) \times \left(\varepsilon_{pot} \times R_s \times T_s \times W_s\right) \tag{6}$$

where APAR is the absorbed photosynthetically active radiation, the product of incoming PAR (≈45% of incoming shortwave radiation) and the NDVI-derived fraction of absorbed PAR (FPAR), and ε is the realized light-use efficiency. ε is obtained from a biome-specific potential efficiency (εpot) down-regulated by scalar functions (0–1) of diffuse radiation (Rs), air temperature (Ts), and vapor pressure deficit (Ws). The FPAR–NDVI relation, the three stress-scalar expressions, and the biome-specific parameters (calibrated against FLUXNET2015) are provided in Supplementary Text S1 and Table S1.

CCW is a carbon-centric model in which ET estimation is constrained by GPP and the underlying water-use efficiency (UWUE; Zhou et al., 2014), which is computed as:

$$ET = \frac{GPP \times VPD^{0.5}}{UWUE} \tag{7}$$

where UWUE (g C $hPa^{0.5}\,kg^{-1}$ H_2O) is the underlying water use efficiency derived from FLUXNET data for each biome (Pastorello et al., 2020). UWUE values range from 4.5 to 8.4 g C $hPa^{0.5}\,kg^{-1}$ H_2O for different biomes (Table S1). This carbon–water coupling is particularly well suited to post-fire analysis. Fire-induced reductions in canopy density suppress GPP and simultaneously reduce ET through the same biophysical linkage, ensuring that disturbance effects propagate consistently through both carbon and water budgets without requiring separate parameterization. Despite its relatively parsimonious structure, this formulation achieves accuracy comparable to more complex process-based models when evaluated against global eddy-covariance data, while remaining directly sensitive to satellite-observed changes in vegetation state (Zhang et al., 2016, 2019).

Water yield (WY) is estimated as the difference between annual precipitation (P) and ET:

$$WY = P - ET \tag{8}$$

This formulation assumes that interannual changes in soil water storage are negligible, an assumption generally supported at annual aggregation timescales. WY therefore represents the annual surplus of precipitation over vegetation water use, the water potentially available for runoff and recharge, and indexes fire-driven changes in ecosystem water use rather than routed streamflow.

2.3.2. Soil erosion estimation

The Revised Universal Soil Loss Equation (RUSLE) was integrated into CCW 2.0 to estimate soil erosion, extending the framework beyond carbon and water fluxes to encompass the geomorphic dimension of post-fire ecosystem disruption:

$$A = R \times K \times LS \times C \times P \tag{9}$$

where A is average annual soil loss (t ha^{-1} yr^{-1}), R is the rainfall erosivity factor, K is soil erodibility, LS is the topographic factor, C is the cover-management factor, and P is the support practice factor.

The rainfall erosivity factor (R) was computed from Daymet monthly and annual precipitation using the Fournier Index. The soil erodibility factor (K) was calculated from POLARIS 30-m soil property data, including sand, silt, clay fractions and organic matter content, following the Wischmeier and Smith (1978) nomograph equation. The topographic factor (LS) was decomposed into slope length (L) and slope steepness (S) components derived from the 30-m DEM and MERIT Hydro contributing area (McCool et al., 1987). The combined LS factor (L × S) captures the interaction of slope length and steepness on erosion potential across GSMNP's complex terrain.

The cover-management factor (C) was estimated dynamically from satellite-observed NDVI following van der Knijff et al. (2000) and Li et al. (2024). For forest land cover classes (NLCD codes 41 to 43), C was rescaled to reflect the enhanced erosion resistance provided by forest litter and root networks, constraining values to the range 0.0001 to 0.04 (Li et al., 2024). This adjustment yields appropriately low erosion rates under intact forest canopies while retaining sensitivity to post-fire canopy loss. The support practice factor (P) was assigned by land cover class, with P = 0.7 for forest, P = 0.9 for grassland, and P = 1.0 for shrublands (Li et al., 2024). Full formulations and parameter values in RUSLE are provided in Supplementary Text S2. Note that RUSLE is a hillslope detachment index whose fire signal is driven by the NDVI-based cover factor; it therefore captures the vegetation-controlled change in erosion susceptibility (relative risk) but, lacking sediment delivery, routing, and channel/mass-wasting processes, does not represent measured sediment export.

2.4. Model running and evaluation

CCW 2.0 generated spatially explicit monthly estimates of GPP, ET, WY, and annual soil erosion at 30-m resolution across 2014 to 2024, with three categories of data input shown below. Satellite-derived vegetation dynamics were represented by HLS-based NDVI at 30-m monthly resolution, which constrained both FPAR and the RUSLE C-factor. Meteorological forcing came from Daymet v4 (Thornton et al., 2022), providing daily minimum air temperature, maximum air temperature, shortwave radiation, precipitation, and VPD at 1-km resolution, bilinearly interpolated to 30 m. Land surface properties included 30-m POLARIS soil texture, MERIT Hydro contributing area, and DEM slope as static inputs, alongside annually updated NLCD land cover classifications to capture post-fire vegetation transitions.

Model performance was evaluated at two independent spatial scales. At the site level, simulated GPP and ET were compared against eddy-covariance flux observations from the NEON deciduous broadleaf forest site in GSMNP (site GRSM; Fig. 1a). The site was only minimally affected by the late 2016 fire, with impacts largely limited to the combustion of surface leaf litter; however, the complete annual records are only available till 2019. Daily flux measurements were aggregated to monthly and annual totals and compared against CCW 2.0 outputs spatially averaged over four candidate footprint radii of 600 m, 900 m, 1500 m, and 3000 m, covering the period 2019 to 2021. At the watershed level, simulated WY and ET were evaluated against USGS streamflow records from the West Prong Little Pigeon River near Gatlinburg, Tennessee (USGS 03469251), a gauging station whose drainage area overlaps the burn perimeter (about 20% of the watershed; Fig. 1a). Mean daily discharge (Q) was aggregated to quarterly and annual totals and converted to WY (mm) by normalizing over the contributing watershed area. Watershed ET was derived from the residual as ET = P - Q, where P is Daymet v4 precipitation aggregated over the same watershed boundary, consistent with the CCW 2.0 formulation. Modeled outputs were then spatially averaged over the watershed and compared against observation-derived estimates for 2023 and 2024, the complete period of record at this station.

Neither the NEON flux record nor the USGS watershed record exhibited a clear fire related signal. These independent observations were therefore used to evaluate the general performance of CCW 2.0 rather than to validate its estimated fire effects. Model performance was assessed using a series of indicators, including the coefficient of determination (R^2), regression slope, *p*-value, and Nash–Sutcliffe efficiency (NSE).

2.5. Factorial simulation design and fire-effect quantification

To separate fire-attributable effects from interannual climate variability, we implemented a factorial simulation design comparing “Fire” and “NoFire” counterfactual scenarios across 2017 to 2024 (Table 1). The Fire scenario, which reflect actual fire impacts and subsequent vegetation recovery, used observed post-fire HLS NDVI time series, annual NLCD and meteorological forcing. The No-Fire counterfactual held vegetation state at the 2016 pre-fire NDVI values and land cover while applying the same year-specific meteorological forcing, representing the ecosystem trajectory we would expect in the absence of disturbance.

Table 1
Factorial simulation design for counterfactual fire-effect attribution. “+" indicates the variable changes dynamically over 2017–2024; "-" indicates the variable is fixed at its pre-fire 2016 level; "–" indicates the variable was fixed at its 2014–2016 pre-fire mean (the seasonal-mean NDVI for the vegetation index, or the annual majority class for land cover).

Simulations	Land Cover	Vegetation Index	Climate
Fire	+	+	+
NoFire	-	-	+
ES1	+	-	+
ES2	-	+	+
ES3	–	–	+

Three extra simulations (ES) were conducted to isolate the drivers of the fire effect and evaluate sensitivity to the baseline choice (Table 1). ES1 held NDVI at its 2016 level while allowing land cover to vary annually, and the NDVI effect was calculated as Fire - ES1. ES2 held land cover at its 2016 condition while allowing NDVI to vary annually, and the land cover effect was calculated as Fire - ES2. ES3 held both NDVI and land cover at their 2014–2016 seasonal/annual mean conditions to assess the sensitivity of the no-fire counterfactual to using either 2016 or the 2014–2016 mean as the baseline. All scenarios used year-specific climate, and all simulations were run at 30-m resolution with stratification by dNBR-derived burn-severity class.

Fire effects were quantified using the counterfactual method (M1) as the primary attribution approach, defined as the relative difference between the Fire and No-Fire simulations:

$$\text{Fire effect (M1)} = [(\text{Fire} - \text{NoFire}) \ / \ \text{NoFire}] \times 100\% \tag{10}$$

By applying identical meteorological forcing to both scenarios, M1 separates fire-induced vegetation change from climate variability and is used throughout as the basis for reporting fire impacts. To test the sensitivity of inferred effects to methodological choice, we compared M1 against two common reference approaches. The neighbor-based method (M2) builds a dynamic spatial reference by scaling unburned buffer-zone observations to pre-fire conditions within each severity class:

$$\text{Reference} = \text{Buffer}_{2017\_2024} \times \left[\text{mean}(\text{Class}_{2014-2016}) \ / \ \text{mean}\left(\text{Buffer}_{2014-2016}\right)\right] \tag{11}$$

$$\text{Fire effect (M2)} = [(\text{Fire} - \text{Reference}) \ / \ \text{Reference}] \times 100\% \tag{12}$$

The before–after method (M3) compares post-fire observations to the 2016 pre-fire baseline:

$$\text{Fire effect (M3)} = \left[\left(\text{Fire} - \text{Prefire}_{2016}\right) \ / \ \text{Prefire}_{2016}\right] \times 100\% \tag{13}$$

M3 conflates fire effects with interannual climate variation, which is particularly problematic for precipitation-sensitive variables such as WY and soil erosion. M2 partially addresses this by using a proximal unburned reference, though it assumes that buffer zones experienced the same climate forcing as burned areas. Comparing all three methods therefore reveals how reference method choice and climate confounding jointly shape inferred fire effects and apparent recovery trajectories. To further validate M1, we applied the same factorial design to the unburned buffer zones surrounding the fire perimeter, where no fire signal should be present; if the counterfactual effectively removes climate-driven and interannual vegetation variability, the Fire and No-Fire simulations should converge there, providing an internal consistency check. Finally, to characterize how recovery unfolded across ecosystem functions, we computed rank correlations of fire impacts among GPP, ET, WY, and soil erosion over 2017–2024.

2.6. Google Earth Engine and python implementation

The complete simulation workflow, encompassing HLS data ingestion, quality filtering, NDVI compositing, gap-filling, CCW 2.0 execution, counterfactual factorial simulations, and fire-effect quantification, was implemented in Google Earth Engine (Gorelick et al., 2017). GEE's cloud computing infrastructure enabled efficient pixel-level processing across the full 30-m burn-severity mosaic over the eleven-year study period and facilitates straightforward extension of the framework to other fire-affected landscapes. All subsequent spatial analysis and visualization were performed locally using Python.

3. Results

3.1. Model evaluation against independent measurements

We evaluated CCW 2.0 with independent observations at two complementary scales, drawing on site-level carbon and water flux measurements from the NEON eddy-covariance tower within GSMNP (Fig. 3) and watershed-scale ET and WY derived from USGS streamflow records, respectively (Fig. 4). At the NEON site, CCW 2.0 reproduced the seasonal dynamics of GPP reasonably well ($R^2 = 0.77$, $P < 0.001$; Fig. 3a and b), with a tendency toward slight overestimation in winter and underestimation of summer peaks that largely offset one another at the annual scale (Fig. 3c). Annual GPP totals agreed closely in 2019 and 2021, falling within 4 to 5% of tower-derived values, while a larger discrepancy of 26% emerged in 2020, attributable to anomalously high tower-derived GPP during autumn of that year (Fig. 3c). Given that eddy-covariance GPP estimates themselves carry roughly 10 to 30% uncertainty arising from u* filtering, gap-filling, and flux-partitioning algorithms (Pastorello et al., 2020), the model-tower differences generally fall within the range of measurement uncertainty. Simulated ET showed stronger seasonal agreement with tower observations ($R^2 = 0.90$, $P < 0.001$; Fig. 3d and e), with interannual differences in annual totals remaining within 1 to 15% across the evaluation period (Fig. 3f).

At the watershed scale (Fig. S3), the model reproduced quarterly ET variability ($R^2 = 0.74$, $P = 0.006$; Fig. 4a and b) and matched annual totals in both years to within 0.3–0.5% (Fig. S3c). WY showed comparable agreement ($R^2 = 0.81$, $P = 0.002$; Fig. 4d and e), with annual totals differing by only 0.1–0.4% from gauge-based estimates (Fig. S3f). Although quarterly offsets were evident in summer ET and WY (Fig. S3b and e), these seasonal mismatches compensated across the water year, yielding sub-1% annual bias in both variables. However, this agreement rests on only two years of data and should be interpreted with caution, as the compensating quarterly offsets may not persist under different climate conditions. Although direct validation of soil erosion estimates against field measurements was not feasible in our study, comparison with independent regional observations in the Discussion suggests that the modeled magnitudes are physically reasonable and broadly consistent with field-based evidence from the southern Appalachians. Overall, CCW 2.0 reproduced observed carbon and water fluxes across site and watershed scales ($R^2 = 0.77$–0.90, NSE = 0.47–0.82), providing a quantitative basis for the fire-effect analyses that follow. We note,

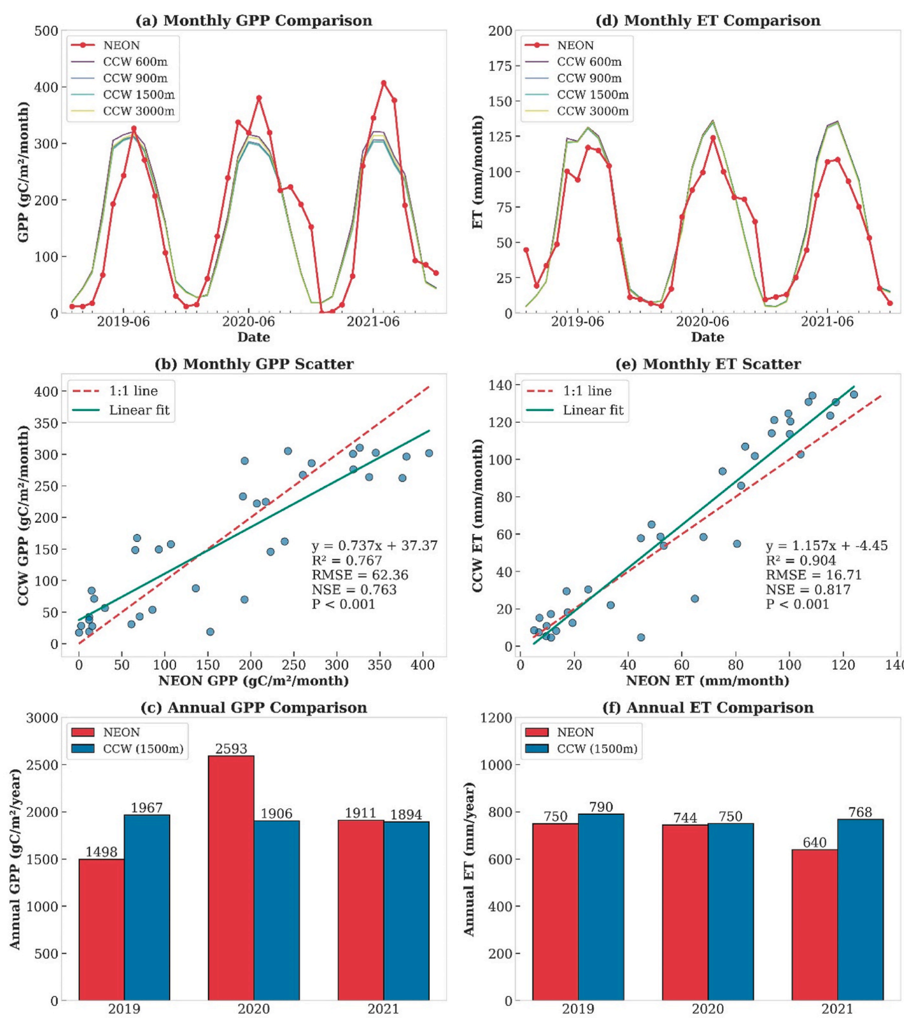

Fig. 3. Site-level evaluation of gross primary productivity (GPP) and evapotranspiration (ET) simulated by CCW against NEON eddy covariance measurements during 2019–2021. **(a)** Monthly GPP time series from CCW simulations at 600, 900, 1500, and 3000 m spatial resolutions and NEON-derived estimates. **(b)** Comparison of monthly GPP simulated at 1500 m with NEON-derived estimates, showing the 1:1 reference line, linear regression, R^2, RMSE, NSE, and *p*-value. **(c)** Annual total GPP from CCW simulations and NEON-derived estimates. **(d)** Monthly ET time series at the four spatial resolutions and NEON-derived estimates. **(e)** Comparison of monthly ET simulated at 1500 m with NEON-derived estimates, showing the same evaluation metrics as in **(b)**. **(f)** Annual total ET from CCW simulations and NEON-derived estimates.

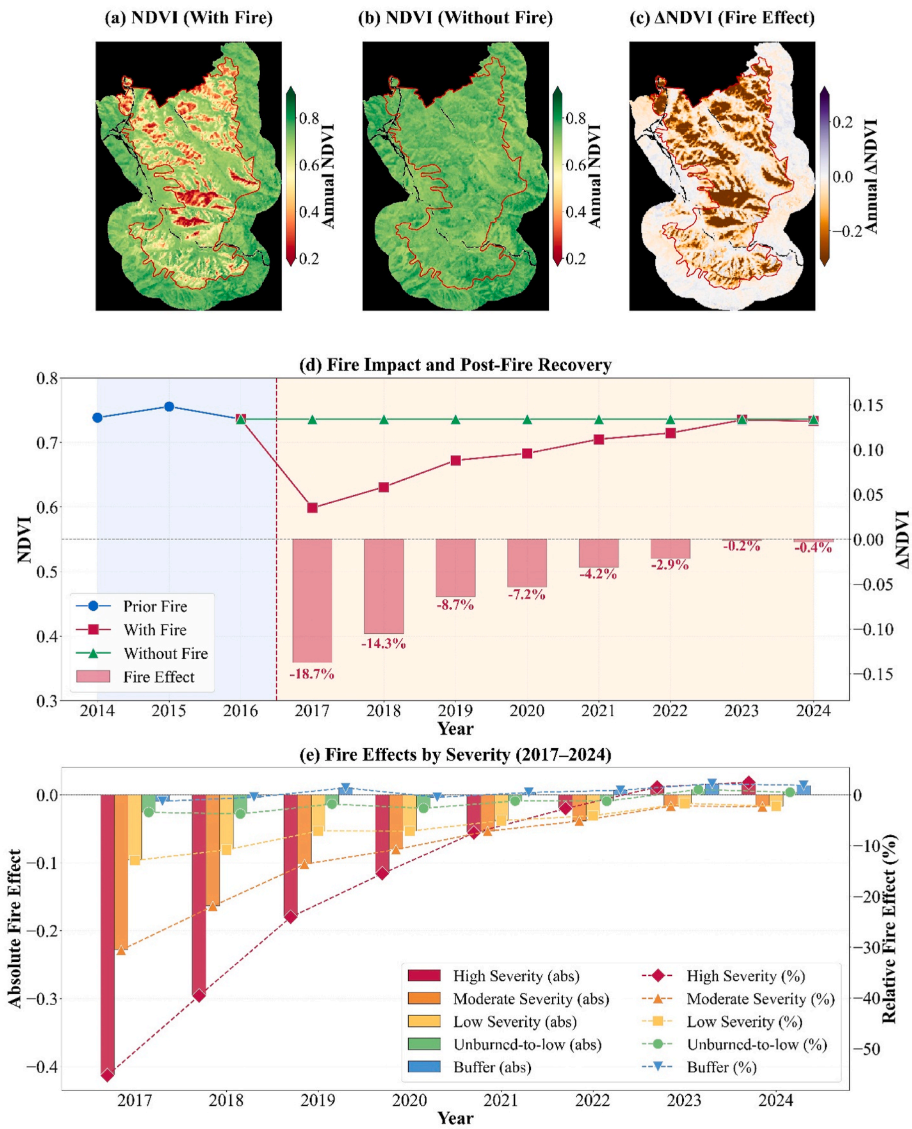

Fig. 4. Spatial patterns and temporal dynamics of fire-induced changes in the normalized difference vegetation index (NDVI). **(a)** Spatially explicit annual NDVI observed under the with-fire scenario. **(b)** Spatially explicit no-fire reference NDVI derived from pre-fire conditions in 2016. **(c)** Fire-induced NDVI anomaly (ΔNDVI = with fire − without fire), with negative values indicating fire-attributable vegetation loss. **(d)** Area-averaged annual NDVI within the fire perimeter from 2017 to 2024 for the with-fire observations and no-fire reference. Bars represent the fire effect (ΔNDVI), and annotations indicate percentage reductions relative to the no-fire reference. The vertical dashed line marks the fire year, and the time series shows the initial vegetation loss followed by gradual post-fire recovery. **(e)** Annual fire effects on NDVI from 2017 to 2024, stratified by burn-severity class (high, moderate, low, and unburned-to-low) and the surrounding buffer zone, expressed as absolute changes (bars) and relative effects (lines).

however, that these evaluations fall well after the fire and therefore carry little information about the early post-fire or high-severity response.

3.2. Fire impacts on eco-hydrological dynamics

Based on counterfactual simulations from CCW 2.0, we revealed substantial immediate fire impacts on multiple eco-hydrological variables (including GPP, ET, WY and SE) that scaled strongly with burn severity, followed by distinct recovery trajectories over the eight-year monitoring period (Figs. 5–8).

3.2.1. Fire severity and its effects on NDVI and land cover change

The 2016 wildfire burned approximately 4615 ha within the study area, with a heterogeneous severity distribution dominated by unburned-to-low severity (43.0%), followed by low (22.1%), moderate (20.7%), and high severity (14.2%) classes (Fig. 1b). High-severity patches were concentrated along upper-elevation ridgelines and south-facing slopes, whereas low-severity and unburned-to-low areas predominated in north faces, valley bottoms and riparian corridors (Fig. 1b), reflecting the combined influence of topography, fuel moisture gradients, and fire weather on burn pattern formation. Annual NDVI across the burned area declined by 18.7% in the first post-fire year (2017) relative to the 2016 pre-fire baseline (Fig. 4a–d). The magnitude of NDVI reduction scaled strongly with NBR-based burn severity (Fig. 4e): high-severity areas experienced the largest absolute decline (approximately −0.40, or ~55% relative reduction), followed by moderate (~31%), low (~13%), and unburned-to-low areas (~3.5%) within the fire perimeter.

This decline in NDVI was mirrored by a shift in land cover (Fig. S2), consistent with canopy loss and structural change across the burn scar. In the years immediately following the fire (2017–2019), forest across the burn scar was reclassified to grass/herbaceous cover, most extensively across the higher-severity portions of the burn where canopy loss

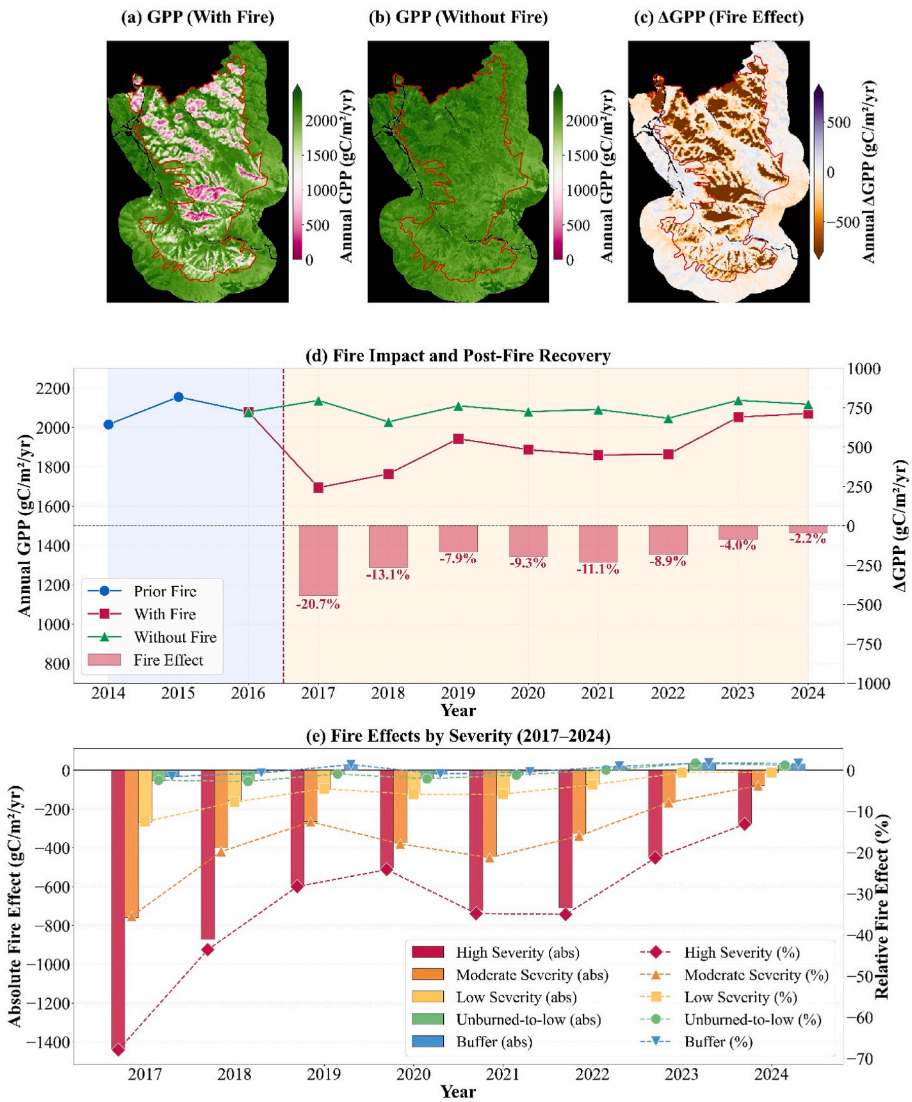

Fig. 5. Spatial patterns and temporal dynamics of fire impact on gross primary productivity (GPP). **(a)** Spatially explicit annual GPP simulated under the fire scenario (With Fire). **(b)** Spatially explicit annual GPP simulated under the counterfactual no-fire scenario (Without Fire). **(c)** Fire-induced GPP anomaly (ΔGPP = With Fire − Without Fire), where negative values indicate fire-attributable productivity losses. **(d)** Annual GPP time series (2017–2024) averaged across the fire perimeter from CCW simulations with and without fire, with bars indicating the fire effect (ΔGPP) and annotated percentage reductions relative to the no-fire scenario; the vertical dashed line marks the fire year, and the trajectory illustrates immediate productivity loss followed by gradual post-fire recovery. **(e)** Annual fire effects on GPP stratified by burn severity class (high, moderate, low, and unburned-to-low) and the surrounding buffer zone (2017–2024), expressed as both absolute changes (bars) and relative effects (lines).

was greatest. As vegetation regenerated, these areas transitioned through a shrub-dominated stage (2020–2022) before returning toward forest by 2023–2024, tracing a successional trajectory from herbaceous to woody cover. The spatial extent and persistence of forest-to-non-forest conversion scaled with burn severity, so that higher-severity patches remained in non-forest classes longest, mirroring the severity-dependent NDVI recovery and providing the structural basis for the delayed functional recovery examined in later sections.

3.2.2. Gross primary productivity (GPP)

Wildfire caused an immediate GPP reduction of 20.7% across the entire burned area in 2017, corresponding to a decline from a counterfactual (no-fire) estimate of ~2100 g C m^{-2} yr^{-1} to a fire-scenario estimate of ~1650 g C m^{-2} yr^{-1} (Fig. 5a–d). GPP recovered progressively over the subsequent seven years, with the fire effect diminishing to −13.1% by 2018 and fluctuating between −8% and −11% during 2019–2023, before reaching a residual deficit of −2.2% by 2024 (Fig. 5d). Counterfactual GPP remained stable at ~2050–2150 g C m^{-2} yr^{-1} throughout the study period, confirming that the observed trajectory reflects fire-induced departure rather than background climate trends (Fig. 5d). The non-monotonic recovery pattern—with a temporary intensification of GPP deficits around 2021–2022—likely reflects interannual climate variability that disproportionately affected the recovering canopy relative to the mature counterfactual forest.

Fire severity strongly regulated both the magnitude and persistence of GPP loss (Fig. 5e). High-severity areas experienced the largest initial reduction (~1200 g C m^{-2} yr^{-1} in 2017, or ~68% relative effect) and retained substantial deficits (~13%) through 2024. Moderate-severity areas showed intermediate impacts (~35% in 2017) and recovered to near-baseline conditions by 2023–2024. Low-severity and unburned-to-low areas within the fire perimeter experienced modest initial reductions (~13% and ~2–3%, respectively) and recovered within the first two to three post-fire years. The buffer zone surrounding the burn perimeter showed negligible GPP departures (<2%) throughout the record. Compared with NDVI (Fig. 4), GPP recovery lagged notably in high-severity areas, suggesting that spectral greenness recovers faster

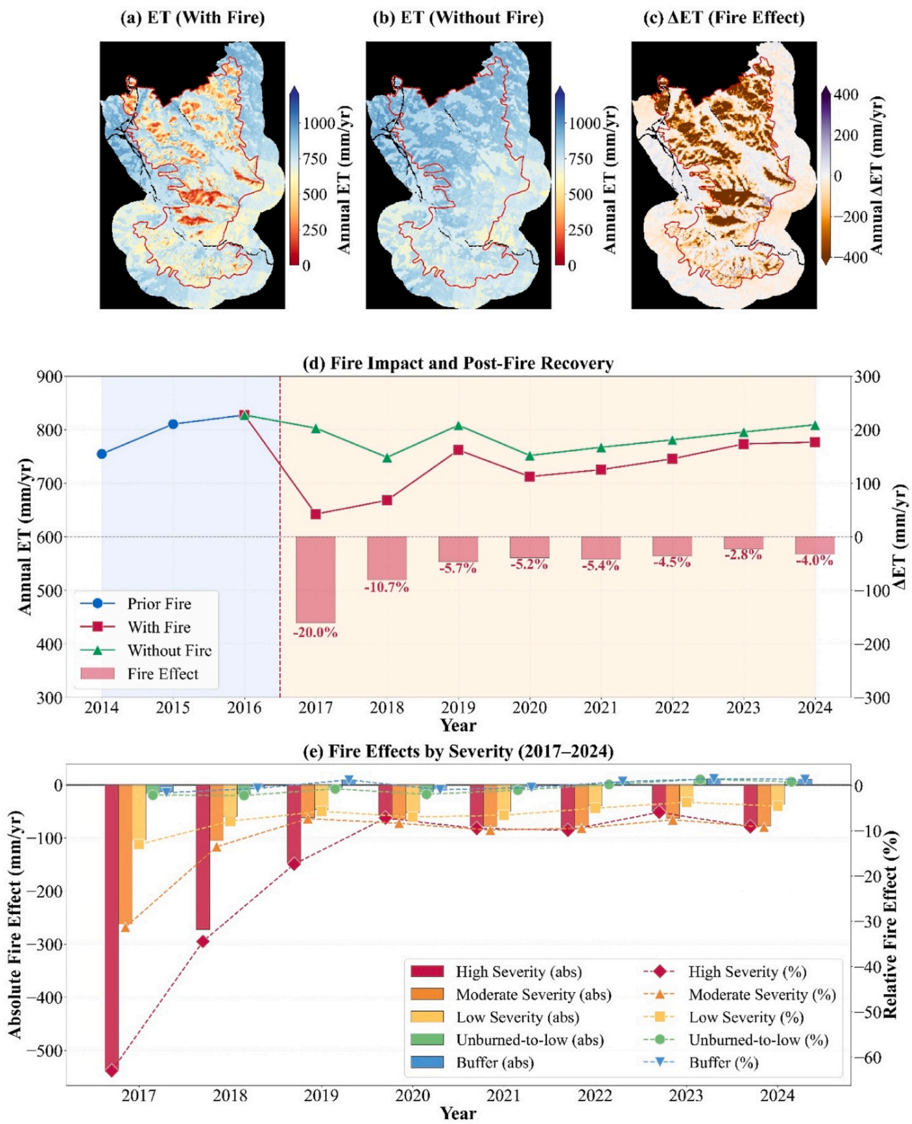

Fig. 6. Spatial patterns and temporal dynamics of fire-induced changes in evapotranspiration (ET). **(a)** Spatially explicit annual ET simulated under the fire scenario (With Fire). **(b)** Spatially explicit annual ET simulated under the counterfactual no-fire scenario (Without Fire). **(c)** Fire-induced ET anomaly (ΔET = With Fire − Without Fire), where negative values indicate fire-attributable reductions in ET. **(d)** Area-averaged annual ET time series (2017–2024) across the fire perimeter from CCW simulations with and without fire, with bars indicating the fire effect (ΔET) and annotated percentage reductions relative to the no-fire scenario; the vertical dashed line marks the fire year, and the trajectory illustrates immediate ET reduction followed by gradual post-fire recovery. **(e)** Annual fire effects on ET stratified by burn severity class (high, moderate, low, and unburned-to-low) and the surrounding buffer zone (2017–2024), expressed as both absolute changes (bars) and relative effects (lines).

than photosynthetic capacity as early successional species (such as serotinous pines) replace the pre-fire canopy.

3.2.3. *Evapotranspiration (ET)*

Fire reduced ET by 20.0% across the burned area in 2017, from ~800 mm yr^{-1} under the counterfactual (no-fire) scenario to ~640 mm yr^{-1} under the fire scenario (Fig. 6a–d). The initial ET suppression was comparable in magnitude to that of GPP (20.7%), reflecting the tight mechanistic coupling between canopy carbon assimilation and evapotranspiration. Because ET was estimated through this carbon–water coupling, the model did not explicitly represent post-fire changes in soil evaporation or canopy interception. The immediate ET response may therefore have been conservative where bare-soil exposure and interception losses changed most abruptly. Recovery was rapid during the first two post-fire years, with the fire effect narrowing to −10.7% by 2018, but subsequently plateaued between −5% and −8% during 2019–2022 before reaching approximately −3% to −4% by 2023–2024 (Fig. 6d), indicating that ET had not fully returned to baseline eight years post-fire. The magnitude and persistence of ET suppression scaled directly with burn severity (Fig. 6e). High-severity areas sustained the largest initial reduction (~500 mm yr^{-1}, or ~63%) and retained losses of ~6–9% through 2024. Moderate-severity areas experienced intermediate impacts (~31% in 2017) and showed continued recovery but retained residual losses of ~7–9% by 2024. Low-severity areas showed initial reductions of ~13% and had not fully recovered by 2024, with residual losses of ~4–5%. Unburned-to-low areas within the fire perimeter experienced negligible initial reductions (~2%) and recovered within one to two post-fire years, while the buffer zone exhibited negligible departures throughout (<2%).

3.2.4. *Water yield (WY)*

Because WY is fundamentally the residual of precipitation minus ET (WY = P – ET), the WY response generally mirrored ET suppression in inverse. Fire increased WY by 19.2% across the burned area in 2017,

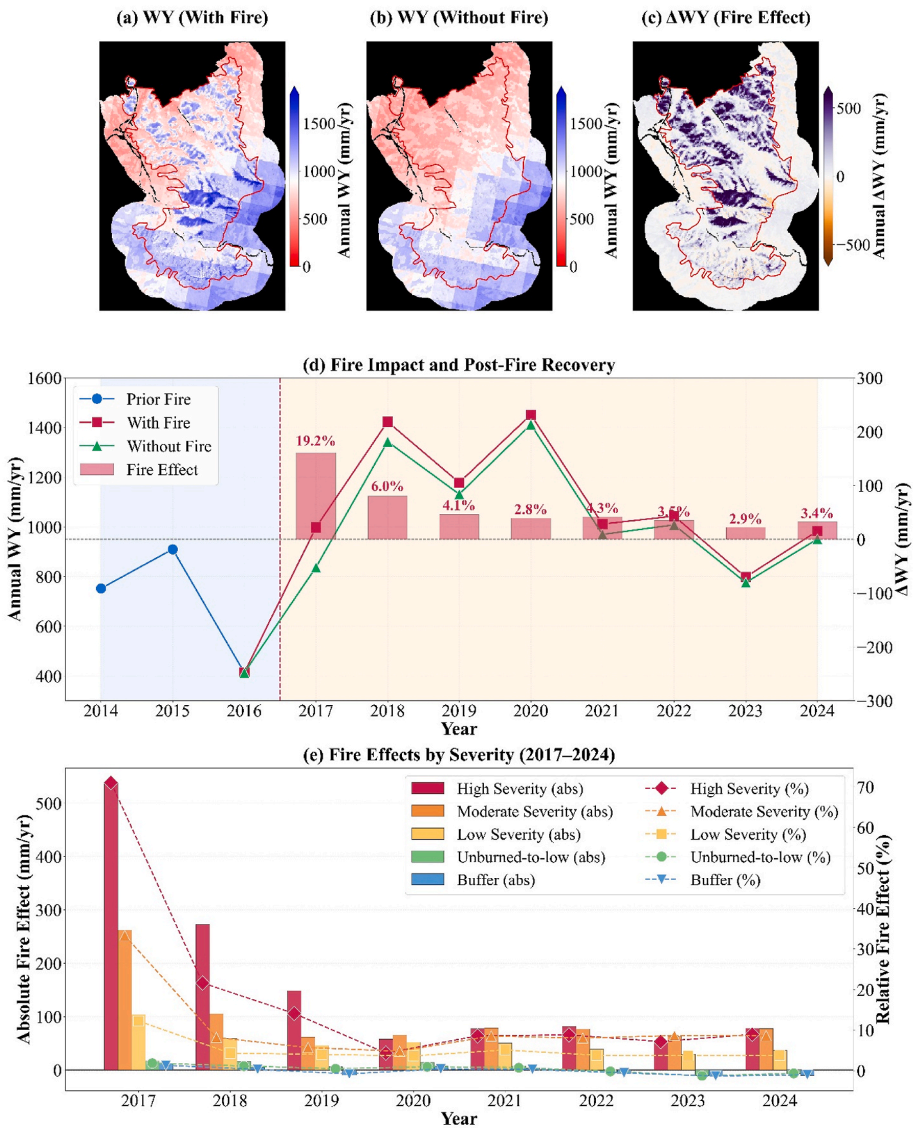

Fig. 7. Spatial patterns and temporal dynamics of fire-induced changes in water yield (WY). **(a)** Spatially explicit annual WY simulated under the fire scenario (With Fire). **(b)** Spatially explicit annual WY simulated under the counterfactual no-fire scenario (Without Fire). **(c)** Fire-induced WY anomaly (ΔWY = With Fire − Without Fire), where positive values indicate fire-attributable increases in water yield. **(d)** Area-averaged annual WY time series (2017–2024) across the fire perimeter from CCW simulations with and without fire, with bars indicating the fire effect (ΔWY) and annotated percentage increases relative to the no-fire scenario; the vertical dashed line marks the fire year, and the trajectory illustrates immediate WY enhancement followed by gradual post-fire recovery. **(e)** Annual fire effects on WY stratified by burn severity class (high, moderate, low, and unburned-to-low) and the surrounding buffer zone (2017–2024), expressed as both absolute changes (bars) and relative effects (lines).

from ~620 mm yr^{-1} under the counterfactual (no-fire) scenario to ~740 mm yr^{-1} under the fire scenario (Fig. 7). Although both observed and counterfactual WY exhibited substantial interannual variability driven by precipitation fluctuations, the counterfactual differencing approach largely cancels out this climate-driven variability, effectively isolating the fire signal. The fire effect declined sharply to +6.0% by 2018 and + 4.1% by 2019, then fluctuated between +2.8% and +4.3% during 2020–2022, before stabilizing at +2.9% to +3.4% in 2023–2024. As with ET, burn severity modulated the magnitude of WY enhancement (Fig. 7e): high-severity areas showed the largest initial increase (~71% in 2017) and maintained elevated yields (~7–9%) through 2024; moderate-severity areas experienced intermediate increases (~33%) that declined initially but persisted at ~8–9% by 2024; low-severity areas showed initial increases of ~12% that diminished to ~4% by 2024; and unburned-to-low areas exhibited minor increases (~2%) that largely disappeared by 2019–2020. The buffer zone showed negligible departures throughout (<2%).

3.2.5. *Soil erosion (SE)*

Fire dramatically amplified soil erosion, with a 12.5-fold increase across the burned area in 2017 relative to the counterfactual, rising from ~3 to ~39 t ha^{-1} yr^{-1} (Fig. 8). This represents by far the largest proportional fire effect among the eco-hydrological variables examined. Erosion declined steadily thereafter but remained substantially elevated throughout the study period: 8.2-fold in 2018, 7.6-fold in 2019, 5.9-fold in 2020, and 2.1-fold by 2024 (Fig. 8d). Even eight years post-fire, soil erosion exceeded baseline rates by more than double, making it the slowest-recovering variable and standing in stark contrast to GPP and ET, which approached near-baseline conditions by 2024. Counterfactual erosion remained stable at ~3–4 t ha^{-1} yr^{-1} throughout the record, confirming that elevated erosion was fire-driven rather than climatically forced.

Burn severity was the dominant control on erosion magnitude and recovery pace (Fig. 8e). High-severity areas experienced the most extreme initial amplification (~48× in 2017) and retained markedly

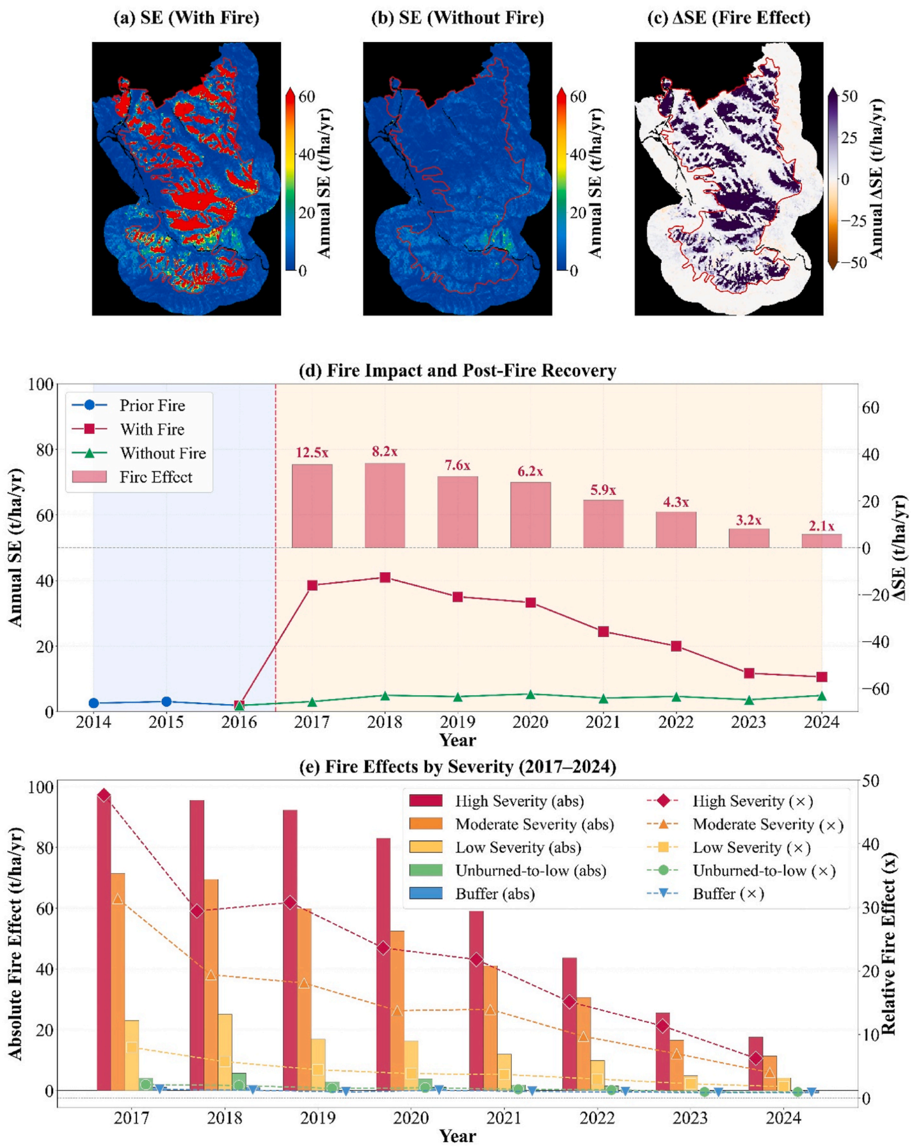

Fig. 8. Spatial patterns and temporal dynamics of fire-induced changes in SE. **(a)** Spatially explicit annual SE simulated under the fire scenario (With Fire). **(b)** Spatially explicit annual SE simulated under the counterfactual no-fire scenario (Without Fire). **(c)** Fire-induced SE anomaly (ΔSE = With Fire − Without Fire), where positive values indicate fire-attributable increases in SE. **(d)** Area-averaged annual SE time series (2017–2024) across the fire perimeter from CCW simulations with and without fire, with bars indicating the fire effect (ΔSE) and annotated changes relative to the no-fire scenario; the vertical dashed line marks the fire year, and the trajectory illustrates immediate SE enhancement followed by gradual post-fire recovery. **(e)** Annual fire effects on SE stratified by burn severity class (high, moderate, low, and unburned-to-low) and the surrounding buffer zone (2017–2024), expressed as both absolute changes (bars) and relative effects (×, lines).

elevated erosion rates (∼6×) through 2024. Moderate-severity areas showed intermediate increases (∼31× in 2017) that declined progressively to ∼4× by 2024. Low-severity areas experienced substantial initial amplification (∼8× in 2017) that declined steadily to ∼1.8× by 2024. Unburned-to-low areas within the fire perimeter showed modest increases (∼2× in 2017) that largely dissipated by 2023–2024, while the buffer zone exhibited negligible departures throughout. The protracted SE recovery relative to NDVI and ET reflects the nonlinear sensitivity of the RUSLE cover-management factor (C-factor) to incomplete canopy closure, whereby even small residual vegetation deficits translate into disproportionately elevated erosion rates.

3.3. Wildfire as a nexus disturbance: coupled eco-hydrological response

Wildfire functions as a nexus disturbance that simultaneously perturbs ecosystem carbon, water, and sediment dynamics through mechanistically coupled pathways (Fig. 9). The conceptual framework (Fig. 9a) illustrates these pathways for high-severity areas across three states: no-fire reference, immediate post-fire disturbance (2017), and late-stage recovery (2024). Under no-fire conditions, intact forest canopies sustain relatively high GPP and ET, moderate water yield, and low soil erosion. Fire-induced canopy and ground cover loss triggered a partially sequential yet interconnected cascade across all four variables. Canopy reduction (NDVI −55%) suppressed GPP by 68% and ET by 63%, which reduced soil moisture drawdown and increased runoff, elevating water yield by 71%. The same canopy and surface cover loss simultaneously removed the physical protection of the soil surface, dramatically amplifying soil erosion by a factor of 47, while the elevated runoff further accelerated sediment mobilization, tightening the connection between the carbon-water and erosion arms of the cascade.

By 2024, vegetation-coupled fluxes showed partial but incomplete recovery, with GPP still 13% below reference and ET 9% below reference, while water yield remained elevated by 9% and soil erosion persisted at five times the reference level. Post-fire recovery rates differed

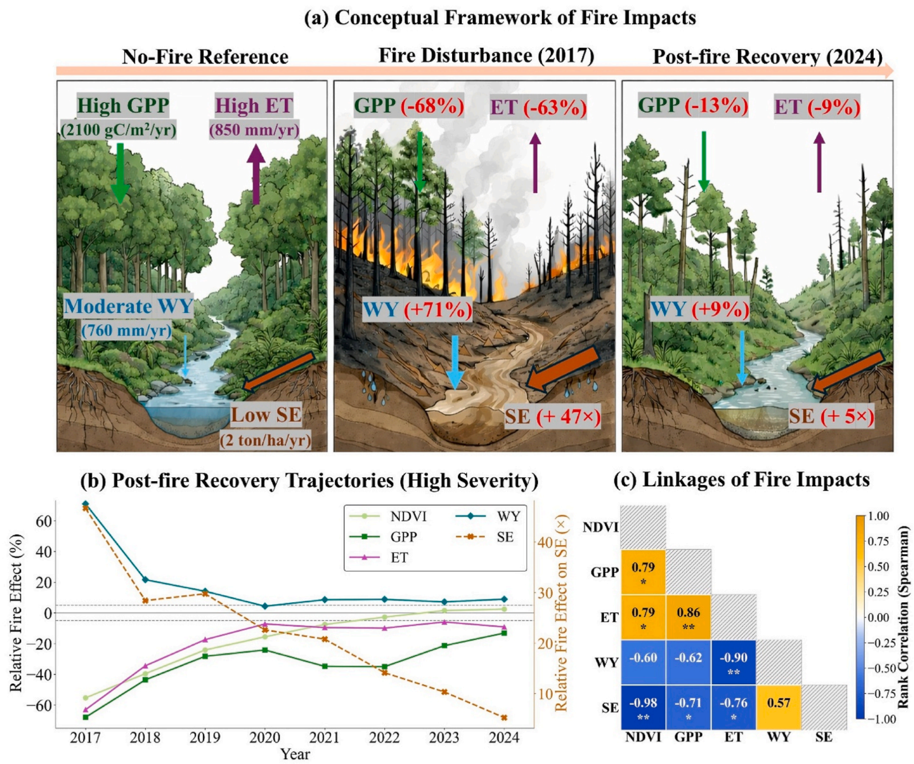

Fig. 9. Conceptual framework and post-fire recovery dynamics in Great Smoky Mountains National Park. **(a)** Conceptual illustration of ecosystem responses in high-severity burn areas across three stages: no-fire reference (2017), fire disturbance (2017), and post-fire recovery (2024); High, moderate, and low in left panel describe pre-fire or no-fire conditions relative to the post-fire state. **(b)** Post-fire recovery trajectories (2017–2024) for NDVI, GPP, ET, WY, and SE expressed as relative fire effects, illustrating rapid initial declines in vegetation productivity and evapotranspiration, gradual recovery over time, sustained water yield increases, and prolonged soil erosion elevation in high-severity areas. **(c)** Rank correlation matrix of fire effects among NDVI, GPP, ET, WY, and SE, indicative of tightly coupled ecohydrological feedbacks following high-severity fire.

substantially across variables (Fig. 9b): NDVI recovered most rapidly, approaching near-baseline by 2022, whereas GPP and ET retained notable losses and SE remained markedly elevated through 2024. Factorial decompositions of these trajectories based on ES2 and ES3 (Table 1) showed that the fire effects were dominated by the NDVI term throughout, but that in the later stage, as NDVI recovered, the land-cover-change term played an increasingly important role in modifying the recovery trajectory and sustaining the residual deficits (Fig. S4).

Functional recovery therefore lags spectral recovery where the post-fire vegetation type differs from the pre-fire forest, showing that spectral recovery alone is an insufficient indicator of functional restoration. The spatial patterns of residual fire effects in 2024 (Fig. S5) further confirm that residual carbon, water, and erosion anomalies concentrate within the high-severity burn areas that underwent the most extensive and persistent forest-to-non-forest conversion (Fig. S5), reinforcing burn severity as the primary spatial determinant of long-term recovery.

Spearman rank correlation analysis of high-severity recovery trajectories (2017–2024, $n = 8$ years) shows that the coupled cascade identified above is reflected in tight vegetation–hydrology–erosion covariation throughout the recovery period (Fig. 9c). Canopy recovery tracked closely with both GPP ($\rho = 0.79$, $p < 0.05$) and ET ($\rho = 0.79$, $p < 0.05$), while the GPP–ET coupling was the strongest pairwise relationship overall ($\rho = 0.86$, $p < 0.01$), and the ET–WY correlation was strongly negative ($\rho = -0.90$, $p < 0.01$). However, because CCW estimates GPP from APAR and light-use efficiency, ET from GPP together with VPD and UWUE, and WY as P − ET (Section 2.3), these carbon–-water correlations partly reflect dependencies built into the model equations and are interpreted here as an internal consistency check rather than as independent evidence that the variables are coupled. The weaker and non-significant correlations of WY with NDVI ($\rho = -0.60$) and GPP ($\rho = -0.62$) suggest that precipitation variability introduces additional noise into the vegetation–water yield linkage beyond what vegetation recovery alone can explain. The strongly negative correlations of NDVI with soil erosion ($\rho = -0.98$, $p < 0.01$) and ET with soil erosion ($\rho = -0.76$, $p < 0.05$) indicate that vegetation recovery exerts primary control over erosion susceptibility, while the positive but non-significant WY–SE correlation ($\rho = 0.57$) indicates that enhanced runoff and elevated erosion share a common driver in canopy loss but their temporal co-evolution is further modulated by rainfall intensity and progressive soil surface stabilization, partially decoupling their trajectories over the recovery period.

3.4. Comparison of fire impacts by three reference methods

We compared fire-effect estimates from the counterfactual method (M1) against the neighbor-based method (M2) and the before-after method (M3) to assess methodological robustness (Fig. 10). All three agreed closely for GPP and ET, with 2017 GPP reductions of 20.7%, 19.5%, and 18.5% for M1, M2, and M3, reflecting the dominance of canopy dynamics over these fluxes. WY was most sensitive to method choice. M3 estimated a 141.4% increase in 2017, roughly seven times the M1 estimate of 19.2%, because its 2016 baseline was an anomalously dry year ($WY = 413\,mm\,yr^{-1}$) and conflated drought recovery with fire-induced change, whereas M2 tracked M1 closely at 18.8%. SE showed intermediate divergence, with M3 estimating 19 times the reference level in 2017 against 11 times for M1 and 9 times for M2, a spread driven by RUSLE's nonlinear sensitivity to small vegetation-index differences and amplified by the very low pre-fire erosion baseline. In contrast, M1 was itself insensitive to the baseline definition, because it applies year-specific climate to both the Fire and No-Fire simulations so that climate variability differences out and only the vegetation effect remains. Substituting the 2014–2016 seasonal mean for the 2016

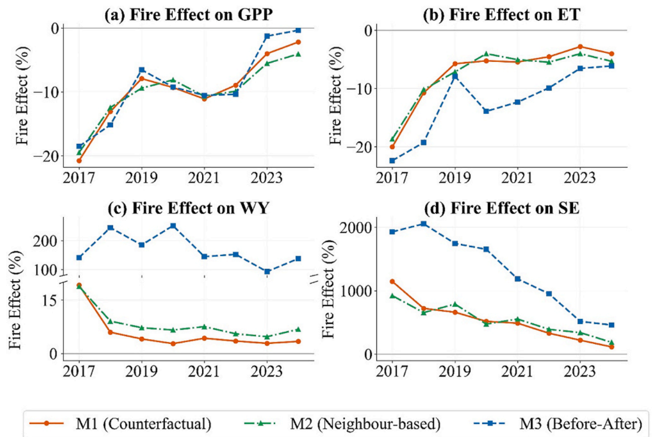

Fig. 10. Comparison of fire impacts on ecosystem carbon and hydrological variables derived from three reference methods. Relative fire effects are shown for **(a)** gross primary productivity (GPP), **(b)** evapotranspiration (ET), **(c)** water yield (WY), and **(d)** soil erosion (SE), each estimated using M1 (counterfactual), M2 (neighbor-based), and M3 (before–after) over the post-fire recovery period (2017–2024). For GPP and ET, negative values indicate fire-induced reductions, while positive values indicate increases relative to the no-fire reference; the reverse applies for WY and SE.

baseline produced nearly identical trajectories, with the only noticeable divergence occurring in the unburned-to-low-severity class, where effect magnitudes are small, demonstrating that the direction, severity ranking, and persistence of the estimated fire effects are robust to the choice of baseline (Fig. S6). Overall, before-after methods risk over- or underestimation when the baseline year is climatically anomalous, and neighbor-based methods can introduce bias from differences between burned and reference areas, while the counterfactual approach provides the most reliable basis for attribution in this study.

4. Discussion

4.1. From spectral indices to functional ecosystem characterization

Our study demonstrates that coupling dense 30-m satellite time series with a diagnostic ecosystem model can bridge the spectral–functional gap in post-fire recovery monitoring across the carbon, water, and soil erosion dimensions. The framework does not replace spectral indices but translates them into physically constrained functional indicators. NDVI-derived greenness and absorbed radiation remain the primary vegetation inputs, but the model reinterprets them through constraints on light-use efficiency, water use, and cover-dependent erosion, so that recovered greenness need not imply recovered function. This distinction matters because post-fire assessments often treat the recovery of spectral indices as evidence of ecosystem recovery, even though vegetation can green up while carbon fluxes, hydrologic function, and soil stability remain impaired (Gitas et al., 2012; Pérez-Cabello et al., 2021).

In the high-severity areas, NDVI returned to near-baseline levels several years before GPP, ET, water yield, and soil erosion showed comparable recovery (Fig. 9). The model reproduces this decoupling because function depends on more than greenness. Once fire converts forest to grass or shrub, the biome-specific parameters governing carbon and water exchange change, so a canopy with recovered NDVI still yields lower modeled fluxes (Figs. S3–S4). This pattern is consistent with growing evidence from other ecosystems, including structural–functional decoupling during post-fire recovery in Eucalyptus forests (Qiu et al., 2026), lengthening prolonged forest recovery times with rising fire severity at the global scale (Lv et al., 2025), and persistent constraints on regeneration and carbon storage decades after stand-replacing fire in Yellowstone (Kiel and Turner, 2022; Kiel et al., 2025). By resolving GPP, ET, WY, and erosion jointly at the 30-m grain of burn-severity mosaics, rather than averaging over severity classes as coarser products do (White et al., 2022), the framework identifies where, and by how much, spectral recovery outpaces functional recovery.

4.2. Severity-dependent recovery and ecological thresholds

Our findings reveal a clear continuum of post-fire ecohydrological recovery strongly governed by burn severity. Low-severity areas largely converged to near-baseline conditions within the study period, with residual effects below 5%, whereas high-severity areas showed no evidence of full functional recovery after eight years despite rapid spectral rebound. This contrast suggests that burn severity acts as an ecological threshold, below which resprouting and canopy closure restore ecosystem function relatively quickly, and above which the system enters a prolonged recovery trajectory that VI-based indicators alone cannot effectively detect.

The rapid low- and moderate-severity recovery are consistent with the strong resprouting capacity of Appalachian hardwoods and pines, supported by preferential carbohydrate allocation to belowground reserves and repeated regeneration after top-kill (Bond and Midgley, 2001; Thompson et al., 2019; K.K. Beals et al., 2022). In the high-severity areas, by contrast, vegetation structure recovered slowly, and by 2024 much of the burn core remained in shrubland rather than returning to forest (Figs. S2 and S5). This incomplete structural recovery underlies the persistent GPP deficit of approximately 13%, since early-successional cover has not yet re-established the canopy structure and physiological functioning of the mature forest it replaced, consistent with evidence that stand-replacing fire can produce decadal recovery horizons, persistent non-forest states (Kashian et al., 2006; Kiel and Turner, 2022; Kiel et al., 2025), and re-greening without functional convergence (Qiu et al., 2026; Vanderhoof et al., 2021; Lv et al., 2025). Warming, regeneration bottlenecks, and disturbance legacies such as nutrient depletion can further delay recovery and promote alternative successional trajectories (Stevens-Rumann and Morgan, 2019; Rodman et al., 2020; Nolan et al., 2021; Pellegrini et al., 2018).

The hydrological and erosional responses revealed by our study are broadly consistent with catchment-scale evidence from the region (Zacharakis and Tsihrintzis, 2026). Fire-driven canopy loss suppresses ET and shifts the water balance toward higher runoff, though detectable water yield gains tend to emerge only when burned extent or high-severity fraction is sufficiently large (Hallema et al., 2018). Paired-watershed observations in the southern Appalachians reported up to 39% greater water yield in burned catchments (Caldwell et al., 2020), and regional analyses found post-fire increases of up to 25% (Bouvier et al., 2025), both generally consistent with our first-year estimate of approximately 19%. Hydrological recovery timescales are contingent on vegetation trajectory, as ET and productivity can rebound within a few years where canopy recovery is rapid (Corak et al., 2026), but elevated discharge can persist for decades when recovery is delayed (Niemeyer et al., 2020; Zacharakis and Tsihrintzis, 2026). Empirical recovery timescales from the southern Appalachians, ranging from four to nine years following clearcutting and land cover conversion at Coweeta (Elliott et al., 2017; Jackson et al., 2018) and approximately five years in burned watersheds (Bouvier et al., 2025), are broadly consistent with our modeled trajectories across burn severity classes. Soil erosion showed the most protracted response, remaining approximately six times above baseline in high-severity areas after eight years, consistent with global RUSLE-based evidence that only about 31% of cumulative post-fire erosion occurs in the first post-fire year (Vieira et al., 2026). Field observations from the region, including 42 times greater storm sediment loss from high-severity relative to low-severity burns (Robichaud and Waldrop, 1994) and in-stream suspended-sediment export of 0.2 to 4.4 t ha^{-1} yr^{-1} following the fire (Caldwell et al., 2020), suggest that our modeled erosion responses are physically reasonable.

Together, these findings imply that spectral index-based monitoring (e.g., NDVI/NBR) may systematically underestimate the duration and cumulative magnitude of post-fire carbon uptake, water-balance shifts, and sediment increase, particularly above the low–moderate severity threshold (Hallema et al., 2017, 2018; Caldwell et al., 2020; Vanderhoof et al., 2021; Vieira et al., 2026). This motivates severity stratified, multidimensional monitoring that goes beyond VI alone to inform post fire habitat and regeneration planning (Stevens-Rumann and Morgan, 2019; Vanderhoof et al., 2021), water supply and watershed risk management (Hallema et al., 2018; Caldwell et al., 2020; Vieira et al., 2026), and disturbance-aware carbon accounting (Harris et al., 2021; Badgley et al., 2022).

4.3. Toward multi-dimensional post-fire ecosystem monitoring: framework, validation, and transferability

Implementing severity-stratified, multi-dimensional post-fire monitoring requires a framework that combines dense satellite observations with diagnostic ecosystem models to track carbon, water, and geomorphic recovery within a common attribution framework (Fig. 9). The NASA HLS product is well suited to this task, providing 30-m surface reflectance at sub-weekly revisit by harmonizing Landsat and Sentinel-2 (Ju et al., 2025). This temporal density supports gap-filled time series that resolve recovery at the scale of burn-severity mosaics, whereas coarser products mix severity classes and weaken attribution (White et al., 2022).

Integrating these time series with CCW 2.0 translates spectral change into carbon fluxes and erosion risk, making it possible to separate areas where green-up reflects genuine functional recovery from areas where it masks continued functional limitation (Kashian et al., 2006; Kiel and Turner, 2022; Kiel et al., 2025; Lv et al., 2025). Such a multi-variable view is essential because post-fire processes are linked but not interchangeable. Canopy loss reduces carbon uptake and evapotranspiration and can raise water yield, while reduced ground cover sustains high erosion risk long after NDVI has recovered, particularly in steep, wet mountain landscapes with high rainfall erosivity (Hallema et al., 2018; Caldwell et al., 2020; Vieira et al., 2026).

CCW 2.0 builds on a modeling framework that first calibrated against global FLUXNET eddy-covariance observations (Zhang et al., 2016) and later extended to global GPP attribution (Zhang et al., 2019), basin-scale water balance analysis (Zhang et al., 2021 Zhang et al., 2021,2022), and regional disturbance-recovery applications (Zhang et al., 2025b). In this study, independent evaluation against NEON eddy-covariance and USGS streamflow observations produced R^2 values of 0.77–0.90 for site-level GPP and ET and 0.74–0.81 for watershed-level ET and water yield. These results extend previous validation to post-fire conditions at 30 m resolution, and the correlation analysis further indicates internal physical consistency among modeled variables (Fig. 9c).

Reliable attribution also depends on how the reference condition is defined. Before-after comparisons can confound fire and climate when the fire year is climatically anomalous, as shown here by the sevenfold overestimation of first-year water yield under that approach. The neighbor-based method reduces this temporal confounding but can introduce spatial bias when burned and reference areas differ environmentally. The counterfactual approach avoids both by generating pixel-level no-fire baselines under identical meteorological forcing, providing the most internally consistent attribution of the three (Hallema et al., 2017). Because the workflow runs in Google Earth Engine using publicly available datasets, including HLS, Daymet, and MTBS, it can be applied directly across fire-affected landscapes in the contiguous United States, and the broader approach transfers to other fire-prone biomes where spectral and functional recovery may diverge, including Australian eucalypt ecosystems (Qiu et al., 2026) and boreal forests (Lv et al., 2025), provided comparable satellite and meteorological inputs are available.

4.4. Protected forests under fire: regional contrasts and management implications

GSMNP is among the most biologically rich temperate protected areas, supporting exceptionally diverse forest communities and providing refuge for numerous rare and endemic taxa within the southern Appalachian biodiversity hotspot. In conservation landscapes of this significance, quantifying both immediate fire effects and long-term recovery is critical, because early post-fire re-greening can mask persistent functional deficits. Our framework meets this need by producing spatially explicit estimates of GPP loss and recovery trajectories at 30 m resolution, allowing managers to identify where productivity losses are greatest, how long deficits persist, and where recovery remains incomplete years after fire. Such information bears directly on restoration prioritization, monitoring of sensitive habitats, and evaluating whether passive recovery is adequate. These capabilities are also relevant for other national parks and protected forests, particularly in western U.S. ecosystems, where post-fire recovery is often slow, spatially heterogeneous, and in some cases fails to return to pre-fire forest conditions, as shown in Yellowstone and other montane landscapes (Kiel and Turner, 2022; Kiel et al., 2025) and in broader regional to global analyses linking increasing fire severity and climate stress to prolonged recovery (Rodman et al., 2020; Lv et al., 2025).

Beyond carbon dynamics, our results underscore the importance of tracking hydrological responses as a coupled disturbance outcome. Even in the eastern U.S., where wildfire risk is generally perceived as lower, severe fire in steep mountain terrain can translate canopy loss into ET suppression, elevated water yield, and accelerated erosion, potentially creating acute downstream hazards (Cui et al., 2018; Rengers et al., 2020). Because the framework diagnoses hillslope erosion potential and a water-balance residual rather than routing water or sediment, its strongest use is to screen and spatially prioritize at-risk areas rather than to predict downstream sediment yield, debris flows, or water-supply volumes. This screening role is consistent with evidence that burned-forest effects on water supply and runoff can be substantial and threshold-like with burned extent and severity (Hallema et al., 2018), and with paired-watershed results in the southern Appalachians showing strong post-fire water-yield and water-quality responses that scale with severity (Caldwell et al., 2020). The same framework transfers directly to western landscapes, where fire is more frequent and hydrologic impacts can persist for years to decades when regeneration is climate-limited; long-term catchment studies document prolonged ET suppression and discharge increases where canopy recovery is delayed (Niemeyer et al., 2020), and climate constraints on recovery are increasingly common (Rodman et al., 2020).

Finally, the framework has clear operational value for planning and adaptive management, not only after wildfires but also for prescribed burning. By mapping severity-stratified sensitivities in GPP, ET/WY, and erosion, the tool can help managers design prescribed fire strategies that meet fuel-reduction or ecological objectives while minimizing eco-hydrological risks to soils and downstream waters, particularly important in regions where prescribed fire is widely practiced (Kolden, 2019; Zhang et al., 2025a). More broadly, because the approach relies on open satellite data (HLS), scalable cloud computation (GEE), and transferable carbon-water-erosion model components, it is well positioned for rapid deployment across other CONUS parks and watersheds and, with appropriate meteorological forcing and regional calibration, for fire-prone regions globally.

4.5. Limitations and future directions

The main limitations arise from simplified representations of post-fire water and soil processes, geographic representativeness, and the spectral and spatial resolution of the input data. In CCW, ET is inferred through carbon–water coupling and does not explicitly partition fluxes into transpiration, soil evaporation, and canopy interception, potentially biasing early post-fire dynamics when bare soil exposure and interception losses change rapidly. Our water yield estimate (WY = P − ET) does not represent soil water holding capacity, storage changes, groundwater exchange, or lateral redistribution, and the framework does not yet incorporate fire-driven changes in soil properties (e.g., hydrophobicity, infiltration capacity, hydraulic conductivity) that alter soil moisture, runoff generation, and erosion response. The RUSLE-based erosion estimates reflect relative hillslope erosion risk rather than fully routed sediment yield, and omit surface sealing and crusting, preferential flow, and channel routing, which can dominate sediment delivery during extreme storms.

The CT2 fire produced high-severity patch sizes atypical of most eastern montane fires, and the deeply dissected terrain of the southern Appalachians is among the most topographically complex in the eastern United States, which may amplify estimated fire effects on water routing and erosion relative to lower-relief landscapes. At 30 m resolution, subpixel heterogeneity in burn severity and vegetation structure may limit sensitivity to fine-scale recovery dynamics, and the broadband indices used here do not resolve the compositional and structural changes that hyperspectral or lidar observations could provide. Future work could improve ET partitioning through two-source schemes, incorporate dynamic soil storage and routing, represent post-fire soil hydraulic changes, and strengthen validation using soil moisture networks, lidar-derived biomass inventories, and sediment, turbidity, and debris-flow datasets. Nevertheless, by leveraging dense, gap-filled 30 m HLS time series, the framework captures first-order, vegetation-driven controls on post-fire carbon, water, and erosion responses and provides spatially detailed, multi-year recovery trajectories at management-relevant scales.

5. Conclusions

We developed a fine-scale post-fire monitoring framework that quantify coupled changes in ecosystem carbon, water, and erosion within a unified attribution approach. Evaluation against NEON eddy-covariance and watershed streamflow observations showed reasonable model performance at both site and watershed scales. Pixel-level counterfactual simulations revealed substantial first-year impacts on ecosystem productivity, evapotranspiration, water yield, and soil erosion. Post-fire recovery trajectories were strongly linked to burn severity, with high-severity areas recovering spectrally by 2022 yet retaining clear carbon, water, and erosion deficits through 2024, suggesting that spectral and functional recovery are decoupled due to the incomplete ecological succession. The framework provides spatially explicit information to support post-fire restoration planning by screening and prioritizing high-severity areas where vegetation monitoring, soil stabilization, and intervention may be most needed; process-complete hydrologic and sediment-routing models would be required for quantitative prediction of streamflow, sediment yield, or downstream hazards. More broadly, the framework offers a transferable approach for moving beyond vegetation-based assessments and tracking both immediate fire impacts and post-fire recovery from local to global scales, with direct implications for understanding how fire shapes long-term carbon uptake, watershed hydrology and the recovery of habitat quality and biodiversity in fire-affected ecosystems.

Declaration of generative AI use

Generative AI tools were used during manuscript preparation for drafting assistance, formatting, code debugging and partial figure generation (i.e., Fig. 9a). All scientific content, analysis design, model development, results interpretation, and conclusions were conducted by the authors. The authors take full responsibility for the content of the publication.

CRediT authorship contribution statement

Yulong Zhang: Conceptualization, Data curation, Formal analysis, Investigation, Methodology, Software, Validation, Visualization, Writing – original draft, Writing – review & editing. **Wenhong Li:** Funding acquisition, Methodology, Project administration, Supervision, Writing – review & editing. **Peter V. Caldwell:** Methodology, Writing – review & editing. **Steven P. Norman:** Methodology, Writing – review & editing. **Conghe Song:** Methodology, Writing – review & editing. **Ge Sun:** Funding acquisition, Investigation, Methodology, Project administration, Supervision, Writing – review & editing.

Declaration of competing interest

The authors declare that they have no known competing financial interests or personal relationships that could have appeared to influence the work reported in this paper.

Acknowledgments

We thank the data providers that made this study possible. HLS data were provided through NASA LP DAAC. Annual land cover data were obtained from NLCD (USGS/MRLC). Meteorological data were obtained from Daymet Version 4 (ORNL DAAC). Burned area and burn severity data were obtained from MTBS (USGS and USDA Forest Service). Flux data were obtained from NEON, streamflow data were obtained from the USGS National Water Information System, and soil property data were derived from the POLARIS dataset. We also acknowledge Google Earth Engine for providing the computing platform used for data processing and analysis.We thank Dr. Chunling Tang from USEPA for her contributions to the methodology and for her review and editing of earlier versions of the manuscript.This research was supported by the USDA Forest Service and the U.S. Environmental Protection Agency through Joint Venture Agreements with Duke University (23-JV-11330180-119; 23-JV-11330180-054). The USDA also supported the contributions of Forest Service employees to this work. The views expressed in this article are those of the authors and do not necessarily represent the views or policies of the U.S. Environmental Protection Agency or the U. S. Department of Agriculture Forest Service.

Appendix A. Supplementary data

Supplementary data to this article can be found online at https://doi.org/10.1016/j.srs.2026.100482.

Data availability

All primary datasets used in this study are publicly available: HLS v2.0 surface reflectance (NASA LP DAAC, https://lpdaac.usgs.gov/products/hlsl30v002/and https://lpdaac.usgs.gov/products/hlss30v002/), Annual NLCD land cover (USGS/MRLC, https://www.mrlc.gov/), Daymet v4 meteorology (ORNL DAAC, https://doi.org/10.3334/ORNLDAAC/2129), the 3DEP/National Elevation Dataset (https://www.usgs.gov/3d-elevation-program) and MERIT Hydro terrain data (https://hydro.iis.u-tokyo.ac.jp/~yamadai/MERIT_Hydro/), POLARIS soil properties (http://hydrology.cee.duke.edu/POLARIS/), MTBS burned-area and perimeter data (https://www.mtbs.gov/), NEON eddy-covariance flux data (site GRSM, https://data.neonscience.org/), and USGS streamflow records (station 03469251, https://waterdata.usgs.gov/monitoring-location/03469251/).

The Google Earth Engine code implementing the key workflow, including HLS filtering and gap-filling, NDVI smoothing, burn-severity classification, the CCW 2.0 Fire and No-fire simulations, the ES1–ES3 factorial experiments, and fire-effect quantification, is shared in the repository users/planetlab/srs_share (folder CT2), accessible at https://code.earthengine.google.com/?

accept_repo=users/planetlab/srs_share.

The model outputs and ancillary spatial layers from 2014 to 2024 are shared as Earth Engine assets under users/planetlab/CT2, accessible at https://code.earthengine.google.com/?asset=users/planetlab/CT2. All layers are at ~30-m resolution, including the five-type fire-scenario simulations, the burn-severity classification, annual reclassified land cover, the fire perimeter. The fire-scenario simulations have 11 bands, including key model inputs (smoothed NDVI and precipitation), eco-hydrological variables (GPP, ET, water yield, soi erosion) and five internal variables for RUSLE. One interactive Google Earth Engine web application is provided for online visualization (https://planetlab.users.earthengine.app/view/ct2fire). It comprises two panels: "Chimney Tops 2 Post-Fire Ecohydrological Patterns," which maps the annual spatial patterns of key ecohydrological fluxes before and after the fire, and "Chimney Tops 2 Fire Impacts and Recovery Trajectory," which shows the fire impacts and post-fire recovery trajectories. The app requires no login, runs in a standard web browser, and will be updated as new data become available.

References

Abatzoglou, J.T., Williams, A.P., 2016. Impact of anthropogenic climate change on wildfire across western US forests. Proc. Natl. Acad. Sci. U. S. A. 113, 11770–11775. https://doi.org/10.1073/pnas.1607171113.

Allen, C.D., Breshears, D.D., McDowell, N.G., 2015. On underestimation of global vulnerability to tree mortality and forest die-off from hotter drought in the Anthropocene. Ecosphere 6, art129. https://doi.org/10.1890/ES15-00203.1.

Badgley, G., Freeman, J., Hamman, J.J., Haya, B., Trugman, A.T., Anderegg, W.R.L., Cullenward, D., 2022. Systematic over-crediting of forest offsets. Glob. Change Biol. 28, 1433–1445. https://doi.org/10.1111/gcb.15943.

Beals, K.K., Scearce, A.E., Swystun, A.T., Schweitzer, J.A., 2022. Belowground mechanisms for oak regeneration: interactions among fire, soil microbes, and plant community alter oak seedling growth. For. Ecol. Manag. 503, 119774. https://doi.org/10.1016/j.foreco.2021.119774.

Beals, S.C., Hartley, I.P., Sherrill, K.R., 2022. Post-wildfire vegetation recovery in the Great Smoky Mountains National Park. Southeast. Geogr. 62, 255–275.

Bond, W.J., Midgley, J.J., 2001. Ecology of sprouting in woody plants: the persistence niche. Trends Ecol. Evol. 16, 45–51. https://doi.org/10.1016/S0169-5347(00)02033-4.

Bouvier, A.B., Clinton, B.D., Vose, J.M., 2025. Post-fire ecosystem recovery in the Great Smoky Mountains: vegetation, soil, and hydrological responses. For. Ecol. Manag. 576, 122380.

Bouvier, I., Caldwell, P., Houser, P., 2025. Spatio-temporal vegetation and catchment dynamics following wildfires in the Southern Appalachian Ecoregion. For. Ecol. Manag. 595, 122996. https://doi.org/10.1016/j.foreco.2025.122996.

Bowman, D.M.J.S., Balch, J.K., Artaxo, P., Bond, W.J., Carlson, J.M., Cochrane, M.A., et al., 2009. Fire in the Earth system. Science 324, 481–484. https://doi.org/10.1126/science.1163886.

Bowman, D.M.J.S., Kolden, C.A., Abatzoglou, J.T., Johnston, F.H., van der Werf, G.R., Flannigan, M., 2020. Vegetation fires in the Anthropocene. Nat. Rev. Earth Environ. 1, 500–515. https://doi.org/10.1038/s43017-020-0085-3.

Bright, B.C., Hudak, A.T., Kennedy, R.E., Braaten, J.D., Henareh Khalyani, A., 2019. Examining post-fire vegetation recovery with Landsat time series analysis in three western North American forest types. Fire Ecol. 15, 8. https://doi.org/10.1186/s42408-018-0021-9.

Caldwell, P.V., Elliott, K.J., Liu, Y., Conner, W.H., Murphy, S.F., Sun, G., McNulty, S.G., Vose, J.M., 2020. Wildfire and prescribed fire effects on streamflow and water quality in the southern Appalachians. Hydrol. Process. 34, 5188–5209. https://doi.org/10.1002/hyp.13922.

Cansler, C.A., McKenzie, D., 2012. How robust are burn severity indices when applied in a new region? Evaluation of alternate field-based and remote-sensing methods. Remote Sens. 4, 456–483.

Chaney, N.W., Minasny, B., Herman, J.D., Nauman, T.W., Brungard, C.W., Morgan, C.L. S., McBratney, A.B., Wood, E.F., Yimam, Y., 2019. POLARIS soil properties: 30-m probabilistic maps of soil properties over the contiguous United States. Water Resour. Res. 55, 2916–2938.

Chen, J., Jönsson, P., Tamura, M., Gu, Z., Matsushita, B., Eklundh, L., 2004. A simple method for reconstructing a high-quality NDVI time-series data set based on the Savitzky–Golay filter. Rem. Sens. Environ. 91 (3–4), 332–344. https://doi.org/10.1016/j.rse.2004.03.014.

Chen, Y., Cao, R., Chen, J., Liu, L., Matsushita, B., 2021. A practical approach to reconstruct high-quality Landsat NDVI time-series data by gap filling and the Savitzky–Golay filter. ISPRS J. Photogrammetry Remote Sens. 180, 174–190. https://doi.org/10.1016/j.isprsjprs.2021.08.015.

Claverie, M., Ju, J., Masek, J.G., Dungan, J.L., Vermote, E.F., Roger, J.-C., et al., 2018. The Harmonized landsat and Sentinel-2 surface reflectance data set. Remote Sens. Environ. 219, 145–161. https://doi.org/10.1016/j.rse.2018.09.002.

Corak, M.J., Wine, M.L., Smoot, E.E., 2026. Distinguishing fire effects from climate variability in post-fire streamflow analysis. Hydrol. Process. 40, e15290.

Corak, N.K., Barros, A.P., Lowman, L.E., 2026. Budyko scatter reveals interactions between wildfire, land cover change, and climate. J. Hydrol. 669, 135096. https://doi.org/10.1016/j.jhydrol.2026.135096.

Cui, Y., Cheng, D., Chan, D., 2018. Investigation of post-fire debris flows in Montecito. ISPRS Int. J. GeoInf. 8, 5.

Eidenshink, J., Schwind, B., Brewer, K., Zhu, Z.-L., Quayle, B., Howard, S.M., 2007. A project for monitoring trends in burn severity. Fire Ecol. 3, 3–21. https://doi.org/10.4996/fireecology.0301003.

Elliott, K.J., Caldwell, P.V., Brantley, S.T., Miniat, C.F., Vose, J.M., Swank, W.T., 2017. Water yield following forest-grass-forest transitions. Hydrol. Earth Syst. Sci. 21, 981–997. https://doi.org/10.5194/hess-21-981-2017.

Gitas, I.Z., Devereux, B.J., Tsakiri-Strati, M., 2012. Burned area mapping and post-fire monitoring. In: Fatoyinbo, T. (Ed.), Remote Sensing of Biomass. IntechOpen. https://doi.org/10.5772/20548.

Gorelick, N., Hancher, M., Dixon, M., Ilyushchenko, S., Thau, D., Moore, R., 2017. Google Earth Engine: Planetary-scale geospatial analysis for everyone. Remote Sens. Environ. 202, 18–27. https://doi.org/10.1016/j.rse.2017.06.031.

Hallema, D.W., Sun, G., Caldwell, P.V., Norman, S.P., Cohen, E.C., Liu, Y., Bladon, K.D., McNulty, S.G., 2017. Assessment of wildland fire impacts on watershed annual water yield: analytical framework and case studies in the United States. Ecohydrology 10, e1794. https://doi.org/10.1002/eco.1794.

Hallema, D.W., Sun, G., Caldwell, P.V., Norman, S.P., Cohen, E.C., Liu, Y., Bladon, K.D., McNulty, S.G., 2018. Burned forests impact water supplies. Nat. Commun. 9, 1307. https://doi.org/10.1038/s41467-018-03735-6.

Harris, N.L., Gibbs, D.A., Baccini, A., Bayer, A., Brown, S., Houghton, R.A., et al., 2021. Global maps of twenty-first century forest carbon fluxes. Nat. Clim. Change 11, 234–240. https://doi.org/10.1038/s41558-020-00976-6.

Jackson, C.R., Webster, J.R., Knoepp, J.D., Elliott, K.J., Emanuel, R.E., Caldwell, P.V., Miniat, C.F., 2018. Unexpected ecological advances made possible by long-term data: a Coweeta example. WIREs Water 5, e1273. https://doi.org/10.1002/wat2.1273.

Ju, J., Zhou, Q., Freitag, B., Roy, D.P., Zhang, H.K., Sridhar, M., Mandel, J., Arab, S., Schmidt, G., Crawford, C.J., 2025. The Harmonized Landsat and Sentinel-2 version 2.0 surface reflectance dataset. Remote Sens. Environ. 324, 114723. https://doi.org/10.1016/j.rse.2025.114723.

Kashian, D.M., Romme, W.H., Tinker, D.B., Turner, M.G., Ryan, M.G., 2006. Carbon storage on landscapes with stand-replacing fires. Bioscience 56, 598–606. https://doi.org/10.1641/0006-3568(2006)56[598:CSOLWS]2.0.CO;2.

Keeley, J.E., 2009. Fire intensity, fire severity and burn severity: a brief review and suggested usage. Int. J. Wildland Fire 18 (1), 116–126.

Key, C.H., Benson, N.C., 2006. Landscape assessment (LA). In: Lutes, D.C. (Ed.), FIREMON: Fire Effects Monitoring and Inventory System. USDA Forest Service Gen. Tech. Rep. RMRS-GTR-164-CD, LA-1–LA-51.

Kiel, N.G., Turner, M.G., 2022. Post-fire canopy recovery and carbon sequestration under alternative stand structures. For. Ecol. Manag. 511, 120135.

Kiel, N.G., Turner, M.G., Smithwick, E.A.H., 2025. Carbon stocks remain depleted 34 years after stand-replacing fire in subalpine forests. Glob. Change Biol. 31, e17605. https://doi.org/10.1111/gcb.17605.

Kolden, C.A., 2019. We're not doing enough prescribed fire in the Western United States to mitigate wildfire risk. Fire 2, 30. https://doi.org/10.3390/fire2020030.

Lv, Q., Chen, Z., Wu, C., Peñuelas, J., Fan, L., Su, Y., Yang, Z., Li, M., Gao, B., Hu, J., Zhang, C., Fu, Y., Wang, Q., 2025. Increasing severity of large-scale fires prolongs recovery time of forests globally since 2001. Nat. Ecol. Evol. 9, 980–992. https://doi.org/10.1038/s41559-025-02683-x.

Lv, Y., Dong, J., Wang, C., Ge, Q., 2025. Global analysis of post-fire vegetation recovery: the role of fire severity and climate. Glob. Change Biol. 31, e17701.

McCool, D.K., Brown, L.C., Foster, G.R., Mutchler, C.K., Meyer, L.D., 1987. Revised slope steepness factor for the universal soil loss equation. Trans ASAE (Am. Soc. Agric. Eng.) 30, 1387–1396.

McDowell, N.G., Allen, C.D., Anderson-Teixeira, K., Aukema, B.H., Bond-Lamberty, B., Chini, L., et al., 2020. Pervasive shifts in forest dynamics in a changing world. Science 368, eaaz9463. https://doi.org/10.1126/science.aaz9463.

Meng, R., Dennison, P.E., Huang, C., Moritz, M.A., D'Antonio, C., 2015. Effects of fire severity and post-fire climate on short-term vegetation recovery of mixed-conifer and red fir forests in the Sierra Nevada Mountains of California. Remote Sens. Environ. 171, 311–325. https://doi.org/10.1016/j.rse.2015.10.024.

Moody, J.A., Shakesby, R.A., Robichaud, P.R., Cannon, S.H., Martin, D.A., 2013. Current research issues related to post-wildfire runoff and erosion processes. Earth Sci. Rev. 122, 10–37. https://doi.org/10.1016/j.earscirev.2013.03.004.

National Park Service, 2022. Chimney tops 2 fire. Great Smoky Mountains National Park. https://www.nps.gov/grsm/learn/chimney-tops-2-fire.htm. (Accessed 29 March 2026).

National Park Service, 2025. Park statistics. Great smoky Mountains national park. https://www.nps.gov/grsm/learn/management/statistics.htm. (Accessed 29 March 2026).

Niemeyer, R.J., Bladon, K.D., Woodsmith, R.D., 2020. Long-term hydrologic recovery after wildfire and post-fire forest management in the interior Pacific Northwest. Hydrol. Process. 34, 1182–1197. https://doi.org/10.1002/hyp.13665.

Nolan, R.H., Collins, L., Leigh, A., Ooi, M.K.J., Curran, T.J., Fairman, T.A., Resco de Dios, V., Bradstock, R.A., 2021. Limits to post-fire vegetation recovery under climate change. Plant Cell Environ. 44, 3471–3489. https://doi.org/10.1111/pce.14176.

Noss, R.F., Franklin, J.F., Baker, W.L., Schoennagel, T., Moyle, P.B., 2006. Managing fire prone forests in the western United States. Front. Ecol. Environ. 4, 481–487. https://doi.org/10.1890/1540-9295(2006)4[481:MFFITW]2.0.CO;2.

Park, T., Sim, S., 2023. Characterizing spatial burn severity patterns of 2016 Chimney Tops 2 fire using multi-temporal Landsat and NEON LiDAR data. Front. Remote Sens. 4, 1096000. https://doi.org/10.3389/frsen.2023.1096000.
Pastorello, G., Trotta, C., Canfora, E., Chu, H., Christianson, D., Cheah, Y.-W., et al., 2020. The FLUXNET2015 dataset and the ONEFlux processing pipeline for eddy covariance data. Sci. Data 7, 225. https://doi.org/10.1038/s41597-020-0534-3.
Pellegrini, A.F.A., Ahlström, A., Hobbie, S.E., Reich, P.B., Nieradzik, L.P., Staver, A.C., et al., 2018. Fire frequency drives decadal changes in soil carbon and nitrogen and ecosystem productivity. Nature 553, 194–198. https://doi.org/10.1038/nature24668.
Pérez-Cabello, F., Montorio, R., Alves, D.B., 2021. Remote sensing techniques for post-fire assessment. In: Manzello, S.L. (Ed.), Encyclopedia of Wildfires and Wildland-Urban Interface (WUI) Fires. Springer, pp. 876–893.
Qiu, T., Anderegg, W.R.L., Mu, M., Flack-Prain, S., 2026. Divergent structural and functional recovery signals in post-fire Eucalyptus forests revealed by multi-source remote sensing. Remote Sens. Environ. 319, 114520.
Reilly, M.J., Norman, S.P., O'Brien, J.J., Loudermilk, E.L., 2022. Drivers and ecological impacts of a wildfire outbreak in the southern Appalachian Mountains after decades of fire exclusion. For. Ecol. Manag. 524, 120500. https://doi.org/10.1016/j.foreco.2022.120500.
Rengers, F.K., McGuire, L.A., Oakley, N.S., Kean, J.W., Staley, D.M., Tang, H., 2020. Landslides after wildfire: initiation, magnitude, and mobility. Landslides 17, 2631–2641.
Robichaud, P.R., Waldrop, T.A., 1994. A comparison of surface runoff and sediment yields from low-severity and high-severity site preparation burns. Water Resour. Bull. 30, 27–34. https://doi.org/10.1111/j.1752-1688.1994.tb03270.x.
Rodman, K.C., Veblen, T.T., Battaglia, M.A., Chambers, M.E., Fornwalt, P.J., Holden, Z. A., et al., 2020. A changing climate is snuffing out post-fire forest recovery in montane forests. Global Ecol. Biogeogr. 29, 2039–2051. https://doi.org/10.1111/geb.13174.
Seidl, R., Thom, D., Kautz, M., Martin-Benito, D., Peltoniemi, M., Vacchiano, G., et al., 2017. Forest disturbances under climate change. Nat. Clim. Change 7, 395–402. https://doi.org/10.1038/nclimate3303.
Smith, H.G., Sheridan, G.J., Lane, P.N.J., Nyman, P., Haydon, S., 2011. Wildfire effects on water quality in forest catchments: a review with implications for water supply. J. Hydrol. 396, 170–192. https://doi.org/10.1016/j.jhydrol.2010.10.043.
Stevens-Rumann, C.S., Morgan, P., 2019. Tree regeneration following wildfires in the western US: a review. Fire Ecol. 15, 15. https://doi.org/10.1186/s42408-019-0032-1.
Thompson, E.G., Coates, T.A., Aust, W.M., Thomas-Van Gundy, M.A., 2019. Wildfire and prescribed fire effects on forest floor properties and erosion potential in the Central Appalachian Region, USA. Forests 10, 493. https://doi.org/10.3390/f10060493.
Thornton, M.M., Shrestha, R., Wei, Y., Thornton, P.E., Kao, S., Wilson, B.E., 2022. Daymet: Daily Surface Weather Data on a 1-km Grid for North America, Version 4 R1. ORNL DAAC. https://doi.org/10.3334/ORNLDAAC/2129.
UNESCO World Heritage Centre, 2012. Great Smoky Mountains National Park. https://whc.unesco.org/en/list/259/. (Accessed 29 March 2026).
van der Knijff, J.M., Jones, R.J.A., Montanarella, L., 2000. Soil Erosion Risk Assessment in Europe. European Commission. EUR 19044 EN.
Vanderhoof, M.K., Hawbaker, T.J., Ku, A., Merriam, K., Berryman, E., Cattau, M., 2021. Tracking rates of postfire conifer regeneration vs. deciduous vegetation recovery across the western United States. Ecol. Appl. 31, e02237. https://doi.org/10.1002/eap.2237.
Vieira, D.C.S., Malvar, M.C., Fernández, C., Serpa, D., Keizer, J.J., 2026. A global synthesis of post-fire erosion rates at the hillslope scale. Earth Sci. Rev. 248, 104890.
White, J.C., Wulder, M.A., Hermosilla, T., Coops, N.C., Hobart, G.W., 2022. Mapping post-disturbance forest recovery at the individual tree level with Planet satellite imagery. Remote Sens. Environ. 271, 112904. https://doi.org/10.1016/j.rse.2022.112904.
Williams, M.D., Johnson, B.D., Cope, Z., Ramseyer, C., Hotz, D., Buckles, J., 2025. Assessing infrastructure exposure to mountain wave wind events in the Southern Appalachians. Nat. Hazards 2, 50. https://doi.org/10.1038/s44304-025-00100-8.
Wine, M.L., Cadol, D., Makhnin, O., 2018. Streamflow increases during post-wildfire recovery across western USA ecoregions. Environ. Res. Lett. 13, 014010. https://doi.org/10.1088/1748-9326/aa9c5a.
Wischmeier, W.H., Smith, D.D., 1978. Predicting rainfall erosion losses: a guide to conservation planning. USDA Agriculture Handbook No. 537.
Xu, H., Chen, H.W., Chen, D., Wang, Y., Yue, X., He, B., Guo, L., Yuan, W., Zhong, Z., Huang, L., 2024. Global patterns and drivers of post-fire vegetation productivity recovery. Nat. Geosci. 17, 874–881. https://doi.org/10.1038/s41561-024-01520-3.
Zacharakis, I., Tsihrintzis, V.A., 2026. Post-wildfire recovery of forest vegetation, soil, and hydrological responses: a review. Earth Sci. Rev., 105452
Zhang, J., Zhang, Y., Dannenberg, M., Guo, Q., Atkins, J., Li, W., Sun, G., 2025b. Eco-hydrological recovery following large vegetation disturbances from a mega earthquake on the eastern Tibetan Plateau. J. Hydrol. https://doi.org/10.1016/j.jhydrol.2024.132595.
Zhang, J., Zhang, Y., Sun, G., Song, C., Dannenberg, M.P., Li, J., Liu, N., Zhang, K., Zhang, Q., Hao, L., 2021. Vegetation greening weakened the capacity of water supply to China's South-North Water diversion project. Hydrol. Earth Syst. Sci. 25, 5623–5640. https://doi.org/10.5194/hess-25-5623-2021.
Zhang, J., Zhang, Y., Sun, G., Song, C., Li, J., Hao, L., Liu, N., 2022. Climate variability masked greening effects on water yield in the Yangtze River Basin during 2001–2018. Water Resour. Res. https://doi.org/10.1029/2021WR030382.
Zhang, Y., Li, W., Caldwell, P., Sebestyen, S.D., Tang, C., Toot, R., Mihiar, C., Mondry, Z., Song, Y., Mosher, D., Sun, G., 2025a. Contemporary patterns of prescribed fire and its risks and benefits to water quantity and water quality over the conterminous United States. Environ. Res. Lett. 20, 123002. https://doi.org/10.1088/1748-9326/ae20af.
Zhang, Y., Song, C., Band, L.E., Sun, G., 2019. No proportional increase of terrestrial gross carbon sequestration from the greening Earth. J. Geophys. Res. Biogeosci. 124, 2540–2553. https://doi.org/10.1029/2018JG004917.
Zhang, Y., Song, C., Band, L.E., Sun, G., Li, J., 2016. Reanalysis of global terrestrial vegetation trends from MODIS products: browning or greening? Remote Sens. Environ. 191, 145–155. https://doi.org/10.1016/j.rse.2016.12.018.
Zhang, Y., Song, C., Hwang, T., Novick, K., Coulston, J.W., Vose, J., Dannenberg, M.P., Hakkenberg, C.R., Mao, J., Woodcock, C.E., 2021. Land cover change-induced decline in terrestrial gross primary production over the conterminous United States from 2001 to 2016. Agric. For. Meteorol. https://doi.org/10.1016/j.agrformet.2021.108609.
Zhou, S., Yu, B., Huang, Y., Wang, G., 2014. The effect of vapor pressure deficit on water use efficiency at the subdaily time scale. Geophys. Res. Lett. 41 (14), 5005–5013. https://doi.org/10.1002/2014GL060741.